NEUROSCIENCE

Gamma oscillation plasticity is mediated via parvalbumin interneurons

Michael D. Hadler[1,2]*, Alexandra Tzilivaki[1,3,4], Dietmar Schmitz[1,3,4,5,6,7], Henrik Alle[1,2], Jörg R. P. Geiger[1,2]*

Understanding the plasticity of neuronal networks is an emerging field of (patho-) physiological research, yet the underlying cellular mechanisms remain poorly understood. Gamma oscillations (30 to 80 hertz), a biomarker of cognitive performance, require and potentiate glutamatergic transmission onto parvalbumin-positive interneurons (PVIs), suggesting an interface for cell-to-network plasticity. In ex vivo local field potential recordings, we demonstrate long-term potentiation of hippocampal gamma power. Gamma potentiation obeys established rules of PVI plasticity, requiring calcium-permeable AMPA receptors (CP-AMPARs) and metabotropic glutamate receptors (mGluRs). A microcircuit computational model of CA3 gamma oscillations predicts CP-AMPAR plasticity onto PVIs critically outperforms pyramidal cell plasticity in increasing gamma power and completely accounts for gamma potentiation. We reaffirm this ex vivo in three PVI-targeting animal models, demonstrating that gamma potentiation requires PVI-specific signaling via a Gq/PKC pathway comprising mGluR5 and a Gi-sensitive, PKA-dependent pathway. Gamma activity–dependent, metabotropically mediated CP-AMPAR plasticity on PVIs may serve as a guiding principle in understanding network plasticity in health and disease.

INTRODUCTION

Cortical networks implement task-specific computations by synchronizing the firing patterns of neurons to a set of defined rhythms, neuronal oscillations (1, 2). Oscillations are distinct regarding both the cortical state that they accompany and the underlying synaptic interactions between the participating neurons (3, 4). Similar to the plasticity of synaptic weights, the spectral amplitude ("power") of distinct oscillatory patterns adapts following learning (5–7) or deteriorates in states of disease (8). Crucially, such changes coincide with either beneficial or detrimental changes in the respective behavioral or cognitive performance. Experimental approaches using either sensory stimuli or optogenetic strategies corroborate the causal link between oscillatory amplitude and cognitive performance on short timescales (9–11) yet fail to explain how these changes are recalled after prolonged periods as required for successful learning. This warrants a cellular storage mechanism of oscillatory response tuning innate to neuronal networks.

Hippocampal gamma oscillations (30 to 80 Hz) contribute to the generation, storage, and retrieval of memories and have been studied extensively in vivo (12, 13), ex vivo (14), and in silico (15). In the CA3 subregion, an understanding has emerged that gamma activity results from precisely timed synaptic feedback loops between local pyramidal cells and interneurons (16–18). Particularly fast-spiking, parvalbumin-positive interneurons (PVIs) are equipped with specific synaptic properties that facilitate synchronization at gamma frequencies, as they quickly transform converging glutamatergic inputs

via GluA2-lacking, calcium-permeable AMPA receptors (CP-AMPARs) into divergent, powerful inhibition (19). During periods of increased neuronal activity, this promotes the co-activation of postsynaptic cells at short time intervals (20, 21), benefiting the induction of synaptic plasticity. In line with this, recent studies have highlighted a vital importance of PVI activation for memory formation and maintenance (22–25). However, it is unclear how this relates to their role in promoting synchrony and further complicated by the fact that PVIs themselves are subjected to various forms of anatomical (26), molecular (27), and synaptic plasticity (28). It is therefore conceivable that PVI plasticity is sufficient to store long-term changes of gamma activity, facilitating its reinstatement upon retrieval.

We previously demonstrated that the induction of network gamma oscillations in vivo and ex vivo evokes long-term potentiation (LTP) of glutamatergic inputs onto both pyramidal cells and PVIs on a cellular level (29). Gamma-induced plasticity is mediated via group I metabotropic glutamate receptors (mGluRs), yet a broader profile of the involved signaling cascades remains to be determined. This prompts the question whether plasticity on a synaptic level affects later overall network activity and, if so, which role is attributed to the specific plasticity obtained by PVIs.

Here, in an ex vivo slice model of murine CA3, we demonstrate that evoked gamma power is markedly increased hours after previous episodes of gamma activity. CP-AMPARs not only are required for the generation of the gamma rhythm but also mediate the subsequent increase of power that we term "gamma potentiation." In an in silico microcircuit model of CA3 gamma oscillations, we predict that an increase of CP-AMPAR conductances at the pyramidal cell–to–PVI synapse completely accounts for gamma potentiation. Using both pharmacological and genetic tools specific to known plasticity rules of PVIs, we confirm that gamma potentiation can be explained entirely by the activation of metabotropic pathways in PVIs and uncover an additional requirement of both protein kinase C (PKC) and protein kinase A (PKA) activation. The cell-to-network transfer of PV input plasticity to output oscillations provides a synaptic basis to gamma frequency–specific network plasticity.

[1]Charité-Universitätsmedizin Berlin, corporate member of Freie Universität Berlin, Humboldt-Universität zu Berlin, Berlin Institute of Health, Charitéplatz 1, 10117 Berlin, Germany. [2]Institute of Neurophysiology, Charité-Universitätsmedizin Berlin, Berlin, Germany. [3]Einstein Center for Neurosciences Berlin, Charitéplatz 1, 10117 Berlin, Germany. [4]Neurocure Cluster of Excellence, Charitéplatz 1, 10117 Berlin, Germany. [5]German Center for Neurodegenerative Diseases (DZNE), Berlin, Germany. [6]Bernstein Center for Computational Neuroscience, Berlin, Germany. [7]Max Delbrück Center for Molecular Medicine in the Helmholtz Association, Robert Rössle-Straße 10, 13125 Berlin, Germany.
*Corresponding author. Email: michael.hadler@charite.de (M.D.H); joerg.geiger@charite.de (J.R.P.G.)

RESULTS

Gamma potentiation in the mouse hippocampus

In acute transverse hippocampal slices of adolescent mice [postnatal day 45 (P45) to P70], we performed multiple single-site local field potential (LFP) recordings in the CA3 pyramidal cell layer. After an initial recording of baseline activity, in which no oscillatory activity was detected, network oscillations in the low–gamma frequency range (25 to 45 Hz, recorded at 32° to 34°C) were reliably induced by bath application of kainate (KA$_1$, 150 nM for 30 min at 1.5 ml/min). Following a 1-hour washout period, during which oscillatory activity had completely subsided after 30 to 40 min, a second, identical period of network activity was induced (KA$_2$, 150 nM for 30 min). During this second application period of KA, peak low gamma power on average increased approximately twofold (Fig. 1A; KA$_1$: 5.66 [1.88, 16.93] μV^2 versus KA$_2$: 11.84 [3.40, 32.50] μV^2, $n = 15$ slices tested; $P = 6.1 \times 10^{-5}$, Wilcoxon signed-rank test). Whereas the absolute values of peak gamma power and frequency in the first induction period were highly variable across individual slices and conditions tested (fig. S1), they did not correlate with the subsequent relative increase of peak power (power KA$_2$/KA$_1$: 2.13 ± 0.11, from here on referred to as gamma potentiation). Across all sole LFP experiments reported in this study, the average potentiation was highly reproducible among control conditions across experimental groups, highlighting the stability of our ex vivo approach (fig. S1).

We confirmed that the increase of peak power was conserved even if the washout period was extended to 3 hours, suggesting a long-lasting change of oscillatory network excitability (Fig. 1, B and C; power KA$_2$/KA$_1$: 2.99 ± 0.71, $n = 10$). However, the overall magnitude of potentiation after 3 hours did not cumulate following two successive application periods of KA, indicating a saturating effect of the first induction period (fig. S2). All subsequently reported potentiation experiments were evaluated after a 1-hour waiting period.

In dual-site recordings, potentiation recorded in CA3 was concomitantly observed in downstream CA1 (fig. S3; CA1 power KA$_2$/KA$_1$: 2.80 ± 0.52, $n = 15$), which in intact slices is synchronized by CA3 in the low–gamma frequency range via the Schaffer collateral pathway (30). In "CA1-Mini" slices, in which CA3 and the subiculum are disconnected from CA1 (31), application of KA evokes rhythmic mid-gamma activity (50 to 60 Hz, recorded at 32° to 34°C). Applying an adjusted application protocol (400 nM KA, 2 × 30 min with 60-min washout) again revealed a roughly twofold increase of peak mid-gamma power (fig. S3; CA1-Mini power KA$_2$/KA$_1$: 1.81 ± 0.12).

These findings suggest a ubiquitous plasticity rule, by which intrinsic gamma activity in CA3 or CA1 induces long-term changes across the local microcircuit and enhances its oscillatory response on repeated identical stimulation. Our finding in transverse CA1-Mini slices, a slice model with reduced recurrent synaptic excitation
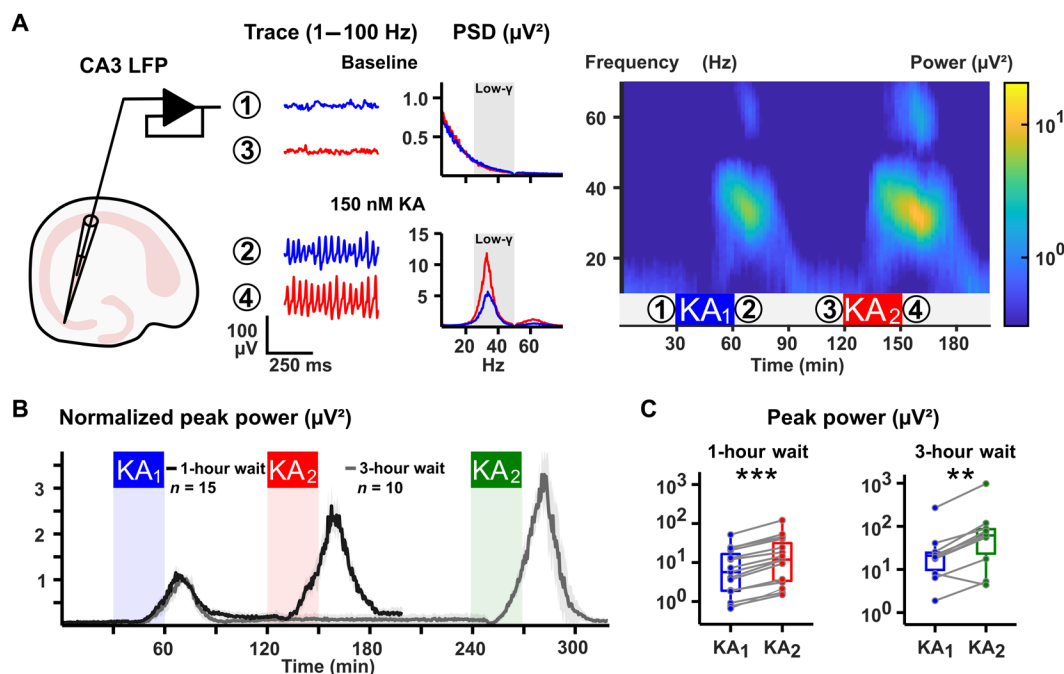
Fig. 1. Gamma potentiation in ex vivo mouse hippocampal CA3. (**A**) Left: Schematic of a hippocampal brain slice with an LFP electrode in the pyramidal cell layer of CA3. Center: Close-up band-pass–filtered traces (1 to 100 Hz) of the time periods preceding KA application (baseline, insets 1 and 3 in the pseudo-color plot) and during maximum gamma power in CA3 ("150 nM KA," insets 2 and 4). The root mean square (RMS)–averaged power spectral density (PSD) was obtained over a 10-min time window. Gray inset low-γ in the PSDs denotes the window spanning from 25 to 50 Hz. Right: Pseudo-color plot of the entire recording. Blue and red insets "KA$_1$" and "KA$_2$" denote the time period of KA application (150 nM). The color bar denotes the RMS-averaged power (log scale). (**B**) Time-power plot of peak power (15 to 49 Hz) for experiments with either 1- or 3-hour delay normalized to the first application period. Ribbons denote the 95% confidence interval. n is number of slices tested. (**C**) Paired boxplots of peak gamma power in both application periods with either 1-hour ($n = 15$) or 3-hour ($n = 10$) delay. **$P < 0.01$ and ***$P < 0.001$ (Wilcoxon signed-rank test).

onto pyramidal cells (*32*), in particular points to plasticity acquired at local pyramidal cell–interneuron interactions.

Calcium-permeable AMPA receptors essentially contribute to the gamma rhythm, mediate and express gamma potentiation

Gamma oscillations arise from synaptic interactions between pyramidal cells and interneurons (*16*). Whereas GABA-mediated transmission is indispensable to oscillogenesis, we could analyze the contribution of individual glutamatergic components to gamma synchronization and its potentiation using pharmacology. To specifically address synaptic excitation onto interneurons, we targeted calcium-permeable AMPA receptors (CP-AMPARs) with the open-channel blocker naphthyl-spermine (NASPM; 50 to 100 μM) and compared this to approaches targeting AMPARs globally (GYKI-53655, 50 μM) and/or NMDARs (D-AP5, 50 μM) (Fig. 2A).

CA3 LFP recordings revealed a fundamental contribution of CP-AMPARs to gamma synchronization: Slices preincubated with NASPM before stimulation with KA exhibited oscillations markedly slower than controls (peak frequency control: 33.12 ± 0.74 Hz, $n = 19$ versus NASPM: 23.09 ± 1.04 Hz, $n = 9$; $P = 9.23 \times 10^{-9}$, generalized linear model), yet clearly synchronous. This decelerating effect was even more pronounced after blocking all AMPARs with GYKI-53655 (peak frequency GYKI: 14.71 ± 0.72 Hz, $n = 9$; $P = 1.75 \times 10^{-19}$ versus control, generalized linear model). Last, co-application of GYKI-53655 and D-AP5, which alone did not affect gamma activity, prevented the emergence of oscillations in eight of the nine slices tested (Fig. 2, B and C). We further confirmed the specific contribution of CP-AMPARs to the generation and maintenance of gamma activity in perforated multielectrode array (pMEA) experiments, permitting short-term drug application. Gamma activity was first established via KA, followed by an intermittent co-application of NASPM. Oscillations quickly desynchronized, quantified as a variable reduction of either peak power and/or frequency, as well as a breakdown of inter-site cross-correlation across CA3 recording sites, which partially recovered following washout of NASPM (fig. S4, A to C). Concerning gamma potentiation, when either GYKI-53655 or NASPM was pre-applied to our LFP protocol, the power of the resulting oscillations did not significantly increase during the second induction period (Fig. 2, D and E; GYKI power KA$_1$: 1.43 [0.90, 9.22] μV^2 versus KA$_2$: 3.89 [1.20, 14.21] μV^2, $n = 9$; $P = 0.10$, Wilcoxon signed-rank test; NASPM power KA$_1$: 16.57 [14.27, 18.52] μV^2 versus KA$_2$: 15.20 [13.79, 19.52] μV^2, $n = 9$; $P = 1.0$, Wilcoxon signed-rank test). D-AP5, on the other hand, had no such effect, with potentiation remaining unchanged (power KA$_2$/KA$_1$ control: 2.58 ± 0.21, $n = 19$ versus D-AP5: 2.38 ± 0.34, $n = 9$; $P = 0.61$, generalized linear model). To exclude a possible contribution of KA receptors, we also tested for effects of UBP-302 (10 μM), an antagonist to the GluK1-subunit. Whereas preincubation with UBP-302 did raise the threshold for gamma oscillation induction (400 nM instead of 150 nM), it did not prevent subsequent plasticity (fig. S5).

The dual role of CP-AMPARs in establishing gamma activity and mediating subsequent network plasticity limited the conclusions of our continuous LFP recordings. Combining our LFP protocol with subsequent pMEA recordings (6×10 grid, 100-μm interelectrode distance) allowed us to observe gamma oscillations at multiple sites covering CA3 and robustly compare independent samples. First, slices were either treated with KA as previously or perfused with

regular artificial cerebrospinal fluid (ACSF) in LFP recordings. Slices were then left to rest for 1 to 3 hours and subsequently placed on pMEAs. In control experiments, both treated and untreated slices were stimulated with KA (200 nM, 3 min at 10 ml/min, 32° to 34°C), inducing low gamma activity (30 to 40 Hz) at sites covering the pyramidal cell layer of CA3c to CA3a (Fig. 3A). For each slice recorded, the electrode recording the highest gamma power was identified as the "lead electrode," variably situated in CA3c, CA3b, or CA3a. In both naïve ("KA$_1$") and treated ("KA$_2$") slices, peak power recorded at sites removed from the lead electrode gradually decreased as a function of intralaminar distance (Fig. 3B, 100 μm to 1 mm). Comparing these distance-based values revealed that, at all sites including the lead electrode, peak gamma power was markedly increased in treated slices compared to untreated slices (Fig. 3C; P values KA$_1$ versus KA$_2$ lead electrode/0 μm, 1.5×10^{-3}; <200 μm, 6.8×10^{-6}; <400 μm, 1.9×10^{-6}; <600 μm, 4.9×10^{-6}; <800 μm, 2.7×10^{-4}; <1000 μm, 2.2×10^{-3}; multiple Mann-Whitney U tests corrected by Holm). Therefore, gamma potentiation is expressed in an activity-dependent manner across the entire CA3 region.

In a separate set of experiments, both naïve and treated slices were perfused with NASPM (100 μM) once placed on the pMEAs and stimulated with KA (Fig. 3D). As observed in our LFP recordings, peak frequencies of both unstimulated (NASPM + KA$_1$) and stimulated slices (NASPM + KA$_2$) were decelerated (17 to 23 Hz) toward control (Fig. 3E) yet comparable in peak power and inter-site synchrony (fig. S4, D and E). However, other than in control recordings (lead electrode power KA$_1$: 8.14 [5.33, 13.16] μV^2 versus KA$_2$: 17.82 [15.84, 20.46] μV^2, $n = 11$; $P = 1.5 \times 10^{-3}$, Mann-Whitney U test), there was no increase of peak power at the lead electrode sites of unstimulated and stimulated slices after NASPM application (Fig. 3F). On the contrary, we observed a trend toward decrease that was not statistically significant (lead electrode power KA$_1$: 17.34 [8.86, 20.79] μV^2 versus KA$_2$: 7.93 [4.15, 15.88] μV^2, $n = 11$; $P = 0.15$, Mann-Whitney U test). Therefore, the increase of peak power is not just induced but also expressed via the activation of CP-AMPARs.

In summary, we could pharmacologically dissect mechanisms of gamma potentiation regarding the ionotropic glutamatergic transmission underlying its induction and expression: Whereas NMDARs and AMPARs contribute differentially to KA-driven oscillations, the generation and subsequent potentiation of gamma oscillations are mediated by AMPARs, expressed specifically by CP-AMPARs in an activity-dependent manner and independent of NMDARs and GluK1. This is strongly indicative of glutamatergic synaptic plasticity onto interneurons (*28*).

A biophysically constrained microcircuit model of CA3 low gamma oscillations predicts superior transfer of PVI-LTP to the resulting field potential

Gamma oscillations induce glutamatergic LTP onto both pyramidal cells (PYR) and predominantly CP-AMPAR–expressing PVIs (*29*). Whereas our pharmacological data suggested that an increase of CP-AMPA conductance at the PYR-PVI synapse underlies gamma potentiation, LTP at the calcium-impermeable AMPAR (CI-AMPAR)–expressing PYR-PYR synapse may, too, directly contribute to changes in the field potential or act heterosynaptically in recruiting PVIs. Lacking experimental tools to selectively target plasticity at PYR-PYR synapses, we turned to an in silico approach using computational modeling.
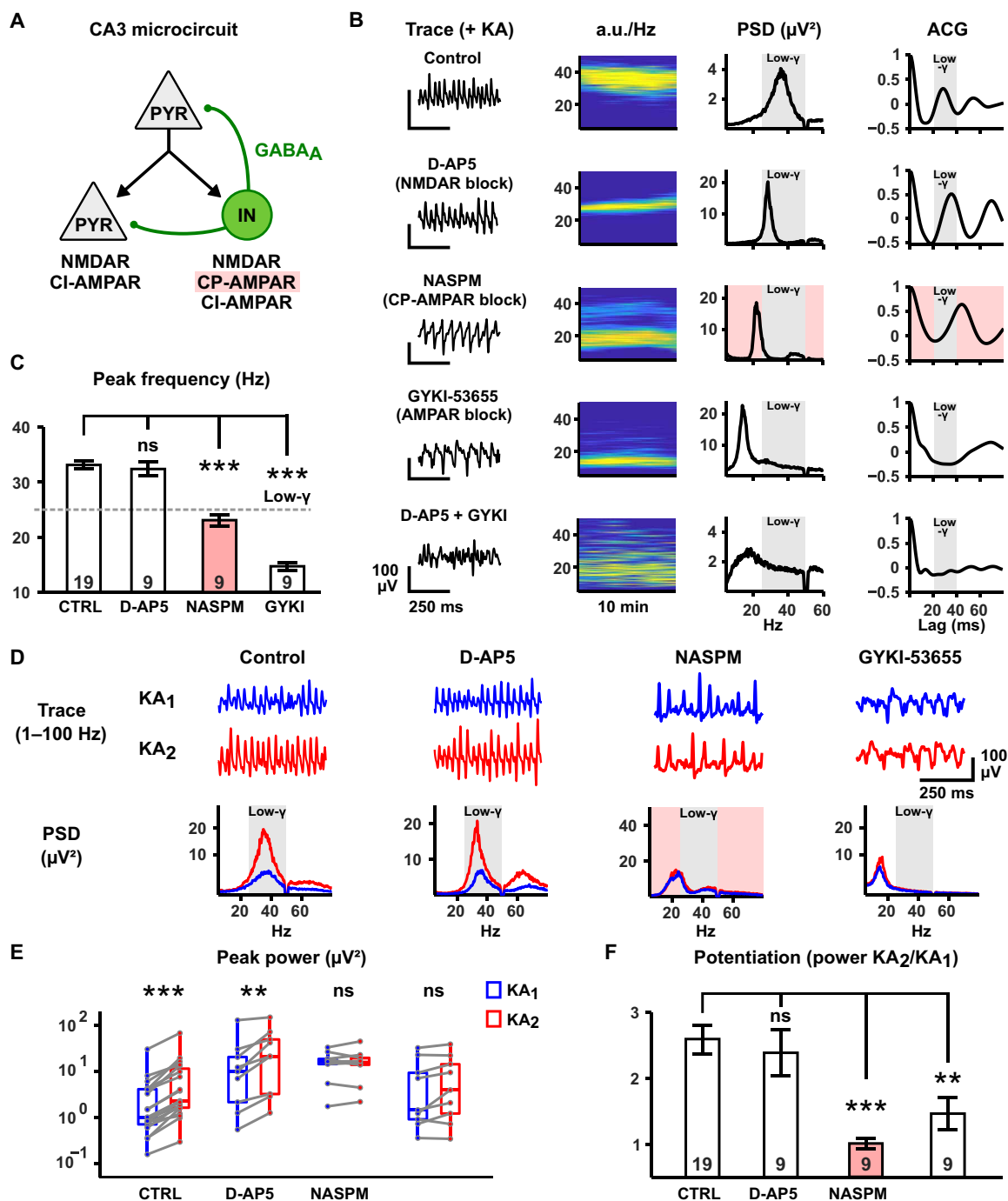
Fig. 2. Calcium-permeable AMPA receptors essentially contribute to the generation of the gamma rhythm and mediate gamma potentiation. (**A**) Synapse-type–specific targeting of glutamatergic transmission in CA3. Pyramidal cell (PYR) synapses targeting other PYRs express NMDA and calcium-impermeable AMPA receptors (CI-AMPARs). PYR synapses targeting interneurons (INs) additionally express calcium-permeable AMPA receptors (CP-AMPARs, pink inset). INs provide inhibition via γ-aminobutyric acid type A (GABA$_A$) receptors. (**B**) Contribution of ionotropic glutamate receptors to KA-induced oscillations. Traces, pseudo-color plots (power values plotted in arbitrary units, "a.u."), PSDs, and autocorrelograms (ACGs) of KA-induced oscillations after blockade of different ionotropic glutamate receptors. Gray insets low-γ in the PSDs and ACGs denote the windows spanning from 25 to 50 Hz and from 20 to 40 ms, respectively. Pink inset highlights the specific blockade of CP-AMPARs by NASPM. There is no discernible oscillatory activity under co-application of D-AP5 and GYKI. (**C**) Barplot summarizing the peak frequencies in the oscillating conditions in (B). Gray dashed line indicates the lower border of the low-γ frequency range (25 Hz). *** $P < 0.001$ (generalized linear model). (**D**) Exemplary potentiation experiments for the oscillating conditions in (B). (**E**) Paired boxplots of respective peak power values during KA$_1$ and KA$_2$ obtained in experiments shown in (D). ***$P <$ 0.001, **$P < 0.01$, and ns (not significant), $P > 0.05$ (Wilcoxon signed-rank test). (**F**) Barplot of the magnitude of potentiation (peak power KA$_2$/KA$_1$) for the experiments in (E). ***$P < 0.001$ and **$P < 0.01$ (generalized linear model). Numbers in barplots denote number of slices tested.
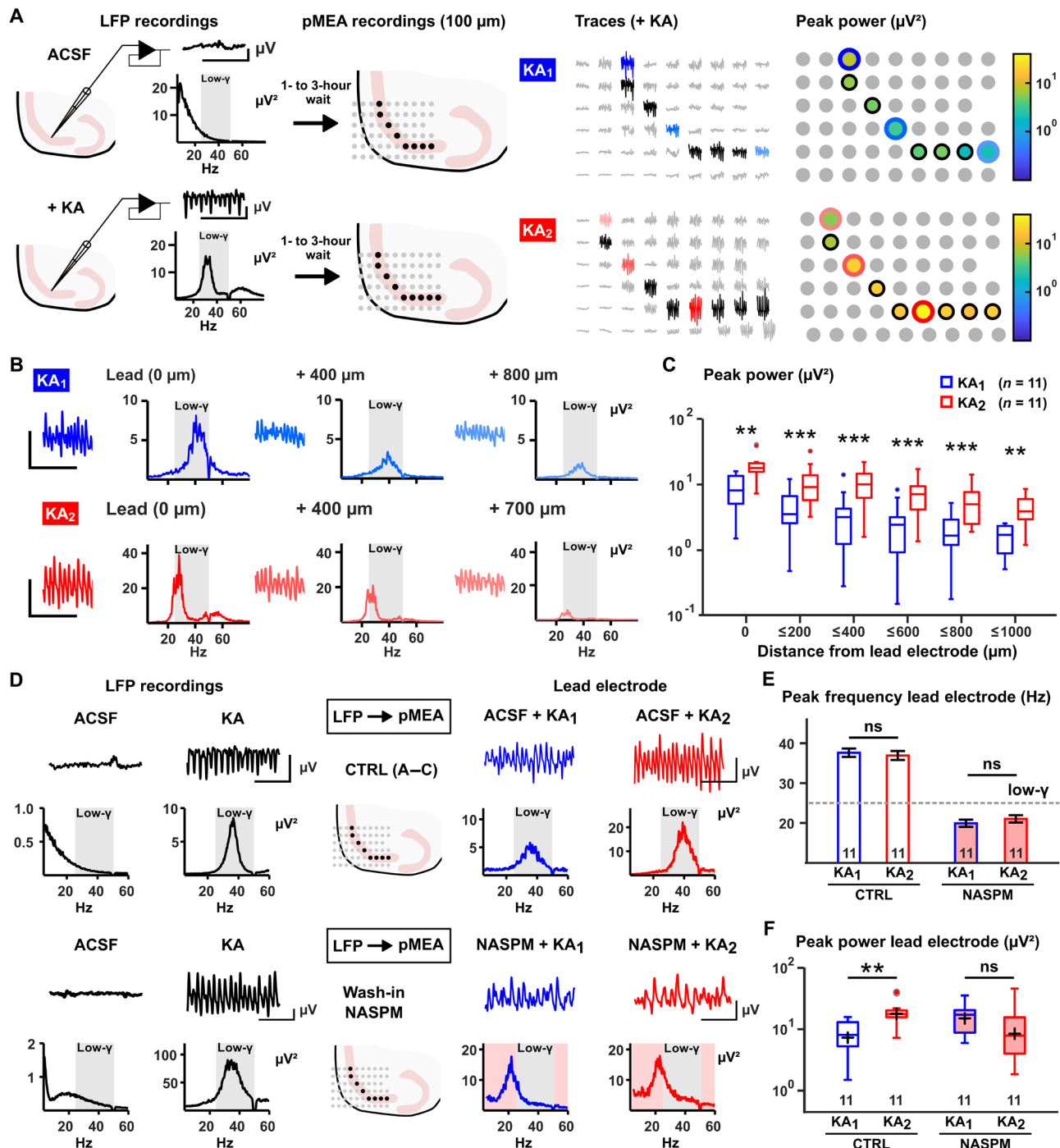
Fig. 3. Gamma potentiation is activity-dependent and expressed via CP-AMPARs. (**A**) Combined LFP-pMEA protocol. Left: In LFP recordings, slices are either left to rest ("ACSF") or treated with KA, yielding low gamma activity. After a waiting period (1 to 3 hours), slices are transferred to pMEAs with the selected electrodes (black) covering the pyramidal cell layer of CA3. KA is applied to untreated (KA$_1$, blue) and treated slices (KA$_2$, red), inducing gamma activity. Right: Heatmaps of peak gamma power over the selected electrodes. (**B**) Exemplary traces and PSDs taken from the experiments in (A). Recordings and corresponding PSDs from the electrodes with the highest power (lead electrode) are compared to those performed at distant sites, illustrating a decrease of peak power over distance. (**C**) Boxplots of peak power in both conditions ($n = 11$ slices tested each) pooled over the intralaminar distance from the lead electrode of each slice. Peak power is increased at all recording sites in treated slices (Mann-Whitney U test, **$P < 0.01$ and ***$P < 0.001$). (**D**) CP-AMPARs express gamma potentiation. Slices were grouped as in (A) and either maintained in regular ACSF ["control ("CTRL"), same dataset as in (A) to (C)] or treated with NASPM on pMEAs before application of KA. The PSD of the lead electrode was calculated for analysis. (**E**) Peak frequency of oscillations is reduced in pMEA "NASPM" conditions. Both treated and untreated slices display peak frequencies under 25 Hz after application of KA ($n = 11$ slices tested in all groups, ns denotes $P > 0.05$, Mann-Whitney U test). (**F**) In CTRL, peak power on the lead electrode is increased in pretreated slices but not in the NASPM condition ($n = 11$ slices tested each). **$P < 0.01$ and ns (not significant), $P > 0.05$ (Mann-Whitney U test).

We developed a microcircuit model of CA3 low gamma oscillations incorporating biophysically constrained, multi-compartmental PYRs ($n = 20$) and PVIs ($n = 2$) and recorded the extracellular "LFP" nearby the pyramidal cell somata. A detailed description of PYR and PVI cellular properties [PVIs adapted from (33)] as well as the model's connectivity configuration can be found in Materials and Methods and table S1 to S3. In this model, a baseline period of low gamma activity can be reliably evoked by introducing an input population selectively targeting the PYR population for 1 s, mimicking our ex vivo approach using KA in a shorter timescale (Fig. 4A; "baseline" power: 29.27 [26.70, 30.42] μV^2). We then simulated LTP at either CI-AMPAR containing PYR-PYR (PYR-LTP) and CP-AMPAR containing PYR-PVI (PVI-LTP) synapses or both synapse types (PYR + PVI-LTP) by increasing their respective conductances by 50% and repeated the otherwise identical simulation (Fig. 4B). The PYR + PVI-LTP condition, which most closely approximated our ex vivo control experiments, reliably resulted in an increase of peak low gamma power by a factor of 2.5 to 3 (Fig. 4, C and D; "PYR + PVI-LTP" power: 89.53 [83.69, 98.01] μV^2, $n = 10$ trials; $P = 1.9 \times 10^{-3}$ versus baseline, Wilcoxon signed-rank test). When simulations were

repeated under identical conditions, yet applying just PYR-LTP, we still observed a significant increase of peak power yet strongly reduced in magnitude (1.15-fold increase; Fig. 4, C and D; "PYR-LTP" power: 34.88 [28.94, 36.53] μV^2, $n = 10$, $P = 1.36 \times 10^{-2}$ vs. baseline, Wilcoxon signed-rank test). In contrast, applying just PVI-LTP to our simulations sufficiently reproduced the increase of power seen in the PYR + PVI-LTP condition, in some cases outperforming it and revealing no additive interaction in combining PYR-LTP with PVI-LTP (Fig. 4, C and D; "PVI-LTP" power: 89.74 [82.70, 93.21] μV^2, $n = 10$, $P = 0.55$ versus PYR + PVI-LTP, Wilcoxon signed-rank test).

Together, our simulations confirm a superior transfer of plasticity expressed at CP-AMPAR containing synapses, formed at PYR-PVI connections, to increasing low gamma power. This is in line with our initial pharmacological data and predicts a substantial contribution of PVI-specific LTP to ex vivo gamma potentiation.

Mechanisms: Gamma potentiation requires PV-specific mGluR5, mGluR1, PKC, and PKA activation

PVI-LTP obtained during gamma oscillations ex vivo can be prevented by unspecific concentrations (50 μM) of the group I mGluR
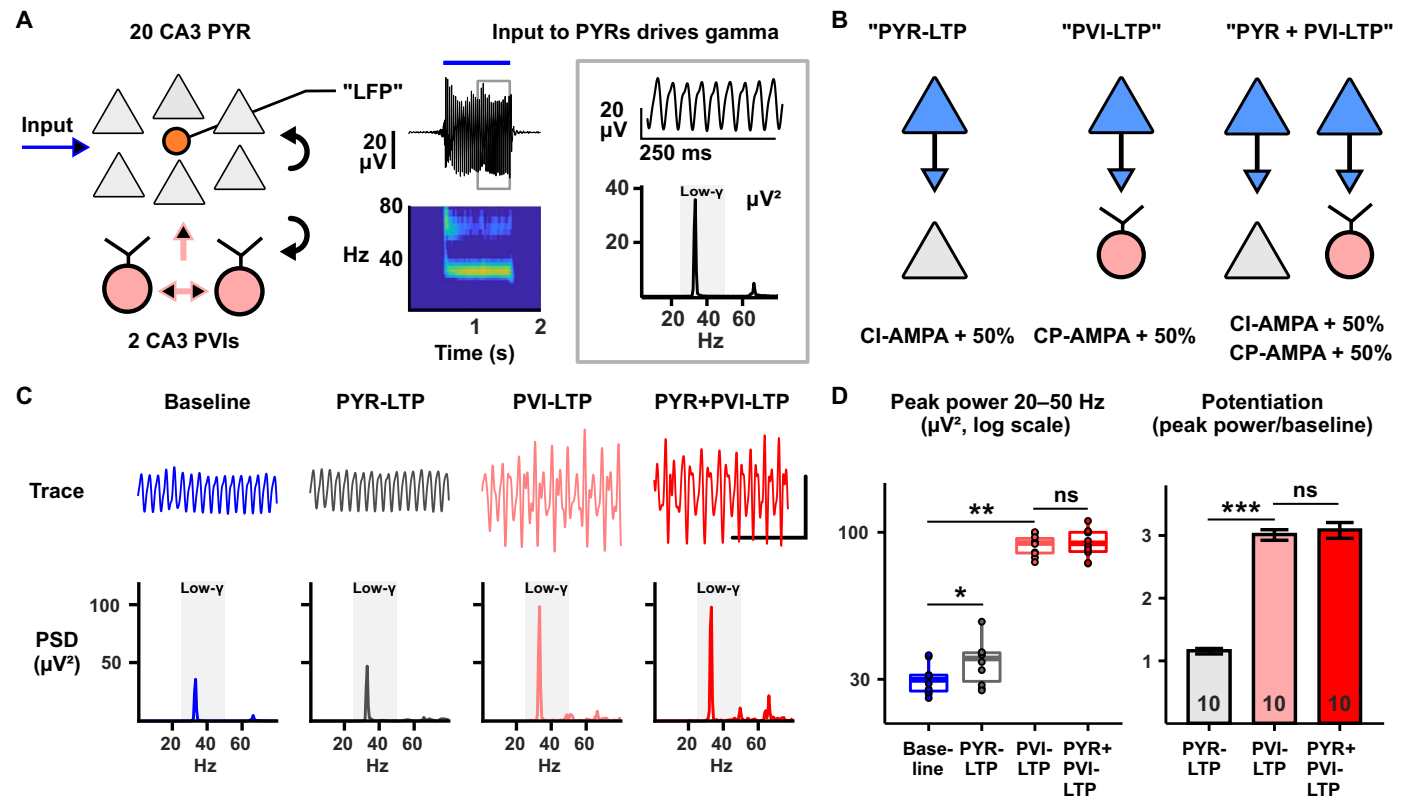

Fig. 4. A biophysically constrained microcircuit model of CA3 low gamma oscillations predicts superior transfer of PVI-LTP to the field potential. (**A**) Left: Microcircuit model of CA3 low gamma oscillations. A population of 20 CA3 pyramidal cells is activated by an input population (blue arrow). The PYR population forms glutamatergic synapses (black arrows) onto PYRs (CI-AMPA and NMDA conductances) and two CA3 PVIs (CP-AMPA and NMDA conductances). The PVIs form synapses onto each other and PYRs with GABAergic synapses (pink arrows). An LFP electrode (orange) is positioned nearby the PYR somata. Center: Exemplary trace of an LFP recording with pseudo-color plot of spectral power below. A 1-s stimulation via the input population produces an oscillation between 30 and 40 Hz. Right: Close-up view of the trace and PSD of the entire 2-s recording. Gray inset marks the low–gamma frequency range (25 to 50 Hz). (**B**) In silico plasticity paradigms. Glutamatergic synapses (blue) formed onto PYRs (gray) and/or PVIs (pink) are modified to simulate cell-type–specific plasticity. CI-AMPA and/or CP-AMPA conductances are increased by 50% for the respective paradigm. (**C**) Traces and power spectra for one exemplary simulation series. Inset denotes 50 μV/250 ms. (**D**) Summary statistics including data from 10 random simulation trials per case. Left: Boxplots of peak low gamma power for all conditions (*$P < 0.05$ and **$P < 0.01$, Wilcoxon signed-rank test). Right: Barplot of the magnitude of potentiation (***$P < 0.001$ and ns, $P > 0.05$, generalized linear model). Numbers in bars denote n = number of simulation trials.

antagonist MPEP (*29*). In an initial set of LFP experiments, we tested the effect of MPEP on gamma potentiation at a concentration specific to mGluR5 blockade (10 µM) as compared to co-application with D-AP5 and found that the magnitude of potentiation was robustly reduced by 50% in both cases (fig. S6). Because of a significant interaction of D-AP5 and MPEP in reducing the average peak frequency of oscillations (by roughly 2 Hz) and a modulating effect of both substances on peak gamma power, all subsequent experiments involving MPEP were performed in the presence of D-AP5 (50 µM).

We next generated mice undergoing Cre/loxp-dependent postnatal ablation of mGluR5 under the PV promoter (*34*), enabling us to assess the cell-type–specific contribution of mGluR5 to gamma potentiation. Slices obtained from these animals ("PV-mGluR5 KO") were compared to those obtained from littermates not expressing the loxp mutation ("PV-mGluR5 WT"), and gamma potentiation was quantified under application of MPEP [Fig. 5A; control (CTRL) versus MPEP]. In both genotypes, gamma oscillations were reliably induced with no apparent difference in peak gamma power between control conditions (Fig. 5B; power KA_1 WT CTRL: 2.38 [0.41, 4.27] μV^2, $n = 16$ versus KO CTRL: 4.00 [1.20, 34.57] μV^2; $P = 0.40$, multiple Mann-Whitney U tests corrected by Holm). Regarding subsequent plasticity, MPEP again attenuated gamma potentiation by approximately 50% compared to wild-type (WT) control slices (Fig. 5, C and D; power KA_2/KA_1 WT CTRL: 2.31 ± 0.21, $n = 16$ versus WT MPEP: 1.49 ± 0.13, $n = 19$; $P = 6.7 \times 10^{-3}$, generalized linear model), confirming our initial results. In slices from PV-mGluR5 KO animals, on the other hand, gamma potentiation was already limited in control slices with no further reduction by MPEP (Fig. 5, C and D; power KA_2/KA_1 KO CTRL: 1.53 ± 0.12, $n = 28$ versus KO MPEP: 1.48 ± 0.11, $n = 19$; $P = 1.0$, generalized linear model). Gamma potentiation in both KO conditions was similarly reduced toward WT control slices as via conventional blockade by MPEP. Moreover, the slightly attenuating effect of MPEP on peak gamma frequency in KA_1 was not observed in KO slices (Fig. 5B). Therefore, the effects of mGluR5 on both gamma activity and subsequent gamma potentiation are mediated specifically via its native expression on PVIs.

mGluR1 coactivation may account for the remaining 50% of gamma potentiation, as both group I mGluRs similarly contribute to CP-AMPAR–mediated PVI-LTP by entraining PKC (*35*, *36*). Beyond such a canonical Gq pathway, PKA or activation of voltage-gated calcium channels (VGCCs), too, contribute to a diverse set of plasticity mechanisms putatively relevant to our paradigm. We tested these assumptions in a set of pharmacological LFP experiments in WT mice (Fig. 5, E to G). First, pre-application of the mGluR1 antagonist JNJ-16259685 (0.3 µM) reduced the magnitude of gamma potentiation toward control conditions [D-AP5, dimethyl sulfoxide (DMSO)] by roughly 50% (Fig. 5E; power KA_2/KA_1 CTRL: 2.13 ± 0.20, $n = 15$ versus JNJ: 1.45 ± 0.11, $n = 16$; $P = 8.1 \times 10^{-3}$, generalized linear model), comparable to sole application of MPEP (power KA_2/KA_1 MPEP: 1.36 ± 0.12, $n = 17$, $P = 1.9 \times 10^{-3}$ versus control, generalized linear model). When both substances were co-applied, we found no residual increase of peak power during the second induction period (MPEP + JNJ peak power KA_1: 34.16 [11.91, 67.14] μV^2 versus KA_2: 35.83 [15.90, 77.57] μV^2, $n = 23$; $P = 0.23$, Wilcoxon signed-rank test), confirming the additive requirement of group I mGluR activation

in our protocol. In a second set of experiments, slices were first preincubated for 1 hour with either the PKC antagonist GF 109203X (GF; 3 µM), the PKA antagonist H-89 (3 µM), or a respective DMSO control (0.01%). Gamma oscillations could be reliably induced in all conditions, whereas oscillations induced following blockade of PKC, but not PKA, displayed a decreased initial peak gamma power (fig. S7). However, both preincubation with GF or H-89 entirely prevented gamma potentiation during the second induction period, demonstrating a requirement of both PKC and PKA activation for gamma potentiation (Fig. 5F; peak power control KA_1: 1.46 [0.77, 6.18] μV^2 versus KA_2: 3.22 [1.64, 9.98] μV^2, $n = 24$, $P = 1.2 \times 10^{-7}$; GF KA_1: 0.30 [0.14, 0.85] μV^2 versus KA_2: 0.41 [0.15, 1.02] μV^2, $n = 20$, $P = 0.18$; H-89 KA_1: 1.40 [0.30, 5.91] μV^2 versus KA_2: 1.58 [0.46, 2.68] μV^2, $n = 25$, $P = 0.62$, Wilcoxon signed-rank tests). Last, when either the L-type VGCC antagonist nifedipine (10 µM) or the T-type antagonist ML-218 (5 µM) was pre-applied, neither the induction of oscillations (fig. S7) nor their subsequent potentiation was significantly affected (Fig. 5G; power KA_2/KA_1 CTRL: 2.07 ± 0.26, $n = 8$; nifedipine: 2.25 ± 0.21, $n = 6$; ML-218: 1.82 ± 0.18, $n = 6$).

This completes a mechanistic profile of gamma potentiation nearly identical to known plasticity rules of glutamatergic LTP onto PVIs: Plasticity of gamma power is independent of NMDARs and VGCCs and instead requires CP-AMPARs, group I mGluRs and PKC (*36*) with an additional requirement of PKA activation. This profile is directly tied to PVIs by the requirement of their cell-type–specific expression of mGluR5.

DREADD-based metabotropic manipulation of PVIs determines the induction of gamma potentiation
Whereas our data from PV-mGluR5 KO slices accounted for the pharmacological effect of MPEP (50% of overall potentiation), open questions remained regarding the residual mGluR1 component and the locus of PKA action. We addressed this by applying two DREADD (Designer Receptors Exclusively Activated by Designer Drugs)-based strategies specific to PVIs and bred mice expressing either the hM4Di-DREADD (*37*) or the hemagglutinin-tagged hM3Dq-DREADD under the PV promoter alongside the fluorescent marker Ai9 ("PV-Ai9-hM4Di" and "PV-Ai9-hM3Dq" animals, respectively). In slices obtained from these animals, the respective DREADD pathway can be reliably activated with the selective compound deschloroclozapine (DCZ) (*38*).

Slices obtained from PV-Ai9-hM4Di animals were preincubated with DCZ (3 µM) before KA application, arguably reducing intracellular cyclic adenosine 3′,5′-monophosphate levels and downstream thereof PKA activity in PVIs (Fig. 6A) (*39*). To preclude nonspecific effects of DCZ, concomitant experiments were performed in mice lacking hM4Di expression ("PV-Ai9"). Neither in slices from PV-Ai9 nor PV-Ai9-hM4Di animals did DCZ affect the induction or maintenance of gamma activity during KA_1 in LFP recordings (Fig. 6B). However, in slices from PV-Ai9-hM4Di animals, subsequent gamma potentiation was completely prevented by DCZ (Fig. 6B; power KA_2/KA_1 PV-Ai9-hM4Di control: 2.37 ± 0.23, $n = 15$ versus DCZ: 1.09 ± 0.10, $n = 15$; $P = 3.4 \times 10^{-6}$, generalized linear model) but not in slices from PV-Ai9 animals (PV-Ai9 control: 2.24 ± 0.23, $n = 13$ versus DCZ: 2.25 ± 0.19, $n = 13$; $P = 0.96$, generalized linear model), indicating that the effect of PKA that we had observed in WT animals can be attributed to its specific activation in PVIs.
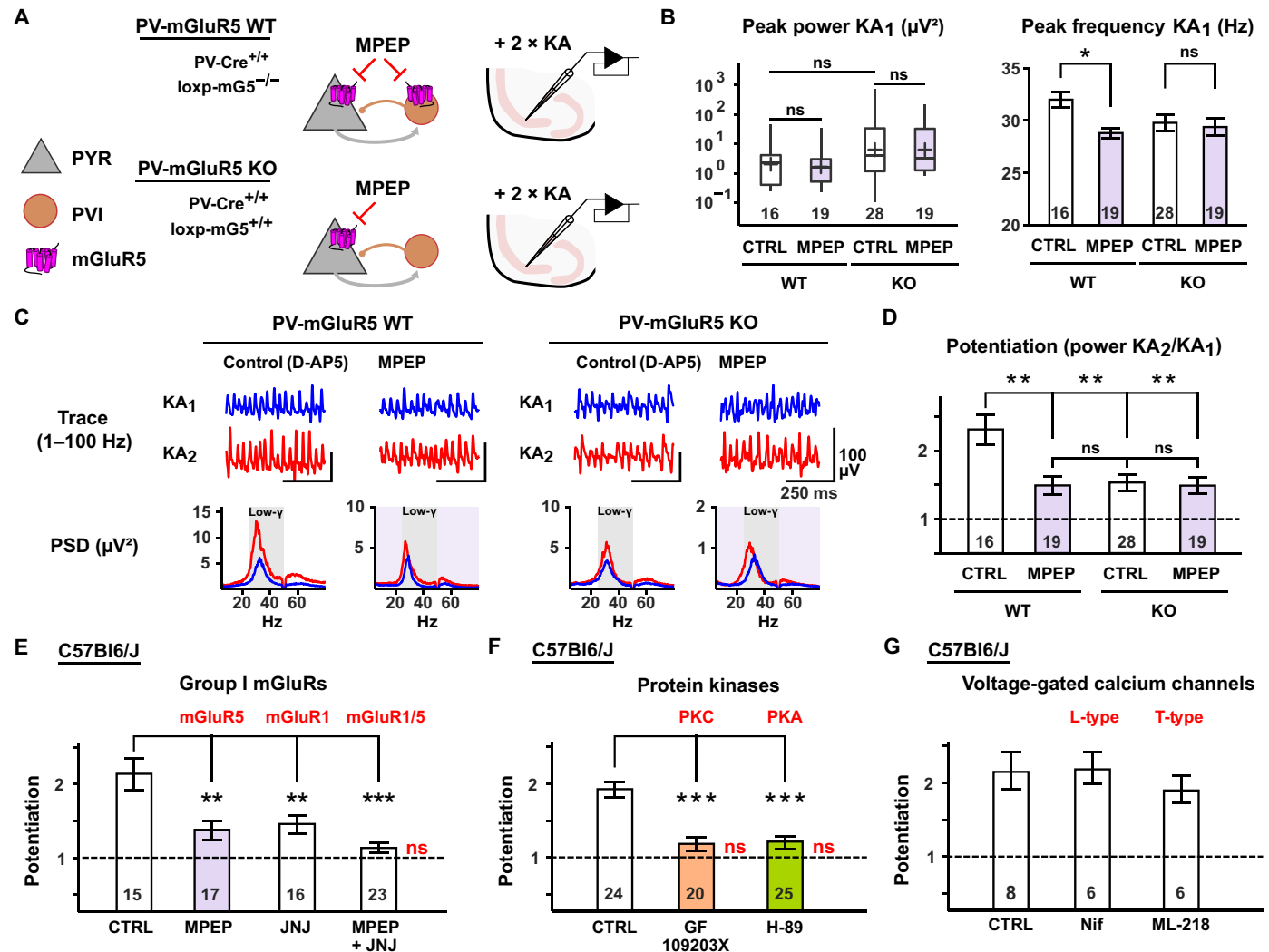
Fig. 5. Gamma potentiation requires PVI-specific mGluR5, mGluR1, PKC, and PKA activation. (**A**) Schematic of PV-mGluR5 experiments. Mice were bred PV-Cre$^{+/+}$ and either lacking (PV-mGluR5 WT) or expressing the loxp-mGluR5 mutation (PV-mGluR5 KO). MPEP blocks mGluR5. Slices from both genotypes were tested with the LFP paradigm. (**B**) Baseline values of KA-induced oscillations under application of MPEP. Left: No differences in peak gamma power ($P > 0.05$, Mann-Whitney U test). Right: MPEP reduces peak frequency in WT, but not KO slices [*$P < 0.05$ and ns (not significant), $P > 0.05$, generalized linear model]. (**C**) Exemplary traces and PSDs of control and MPEP conditions in WT and KO slices during the first (KA$_1$) and second (KA$_2$) induction period, performed in D-AP5 (50 μM). (**D**) Average potentiation in (C). Potentiation is reduced in KO slices with no additional effect of MPEP (**$P < 0.01$ and ns, $P > 0.05$, generalized linear model). (**E** to **G**) Pharmacological profile of gamma potentiation in slices from wild-type (WT; C57Bl6/J) animals. (**E**) Average potentiation under blockade of mGluR5 (MPEP, 50 μM), mGluR1 (JNJ-16259685, "JNJ," 0.3 μM), or both, performed in D-AP5 (50 μM) and dimethyl sulfoxide (DMSO; 0.01%). (**F**) Average potentiation under blockade of PKC (GF 109203X, 3 μM) or PKA (H-89, 3 μM), performed in DMSO (0.01%). (**G**) Average potentiation under blockade of L-type (nifedipine, "Nif," 10 μM) or T-type calcium channels (ML-218, 5 μM), performed in DMSO (0.01%). Red insets "ns" in barplots indicate no increase of peak power in KA$_2$ ($P > 0.05$, Wilcoxon signed-rank test; power KA$_2$ versus KA$_1$). Numbers in plots denote n = number of slices tested. (E) and (F) ***$P < 0.001$, **$P < 0.01$, and ns, $P > 0.05$ (generalized linear model). Purple, orange, and green insets mark the application of MPEP, GF, and H-89, respectively.

In slices from PV-Ai9-hM3Dq animals, we applied the inverse strategy: If gamma potentiation is prevented by blockade of endogenous Gq receptors or PKC, activation of the xeno-receptor hM3Dq in PVIs may be sufficient to rescue blockade of the mGluRs, yet not blockade of downstream PKC (Fig. 6C). On the other hand, hM3Dq activation and subsequent depolarization of PVIs independent of PKC may itself drive PVI firing and thus induce gamma activity, as has been shown for optogenetic strategies (9). We tested these assumptions in multiple steps: First, when applied by itself, DCZ was

insufficient to induce any form of network synchronization, highlighting the requirement of synaptic excitation we had demonstrated earlier (fig. S8). Second, when mGluR5 and mGluR1 were blocked with MPEP (10 μM) and JNJ-16259685 (0.3 μM), gamma potentiation was again prevented in slices from PV-Ai9-hM3Dq animals (power KA$_2$/KA$_1$ PV-Ai9-hM3Dq control: 2.31 ± 0.15, $n = 14$ versus MPEP + JNJ: 1.10 ± 0.16, $n = 12$; $P = 7 \times 10^{-5}$, generalized linear model). This was entirely rescued when DCZ was co-applied with KA, with the magnitude of potentiation nearly identical
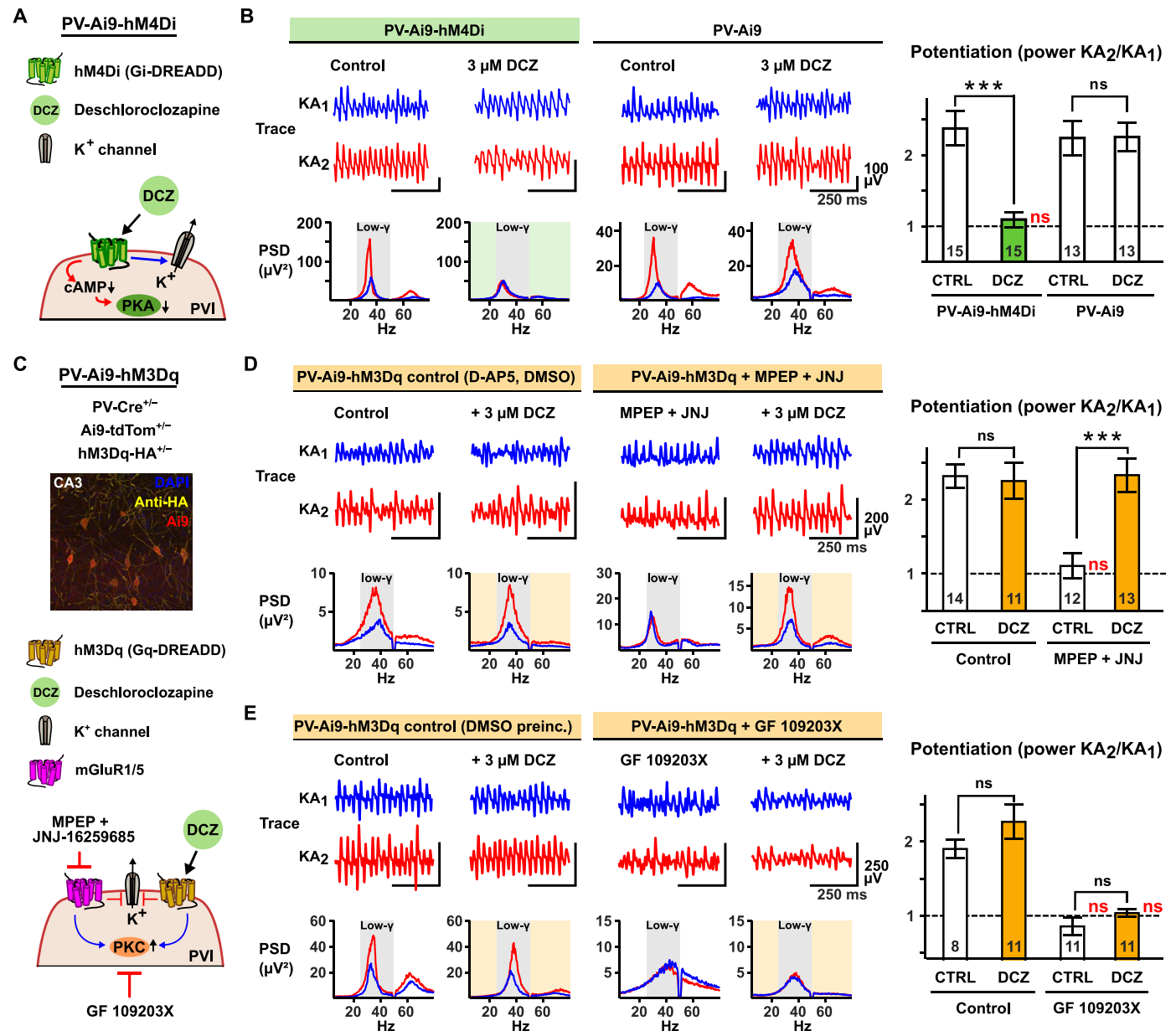
Fig. 6. PVI-specific DREADD manipulations determine the induction of gamma potentiation. (**A**) Schematic of PV-Ai9-hM4Di model. Deschlorocloozapine (DCZ) activates hM4Di in PVIs, reducing intracellular cyclic adenosine 3′,5′-monophosphate (cAMP) and PKA activity and activating potassium channels. (**B**) DCZ prevents gamma potentiation in PV-Ai9-hM4Di slices. Left: Exemplary traces of Control and DCZ conditions for both genotypes during the first (KA_1) and second (KA_2) induction period. Corresponding PSDs below. Right: Barplot of average potentiation. (**C**) Above: Hemagglutinin (HA)–tagged hM3Dq is expressed in CA3 PVIs in PV-Ai9-hM3Dq animals (blue: DAPI, 4′,6-diamidino-2-phenylindole, yellow: HA-tag from Cell Signaling Technology, 3724S, RRID:AB_1549585, ×30 magnification, red: Ai9). Below: Schematic of PV-Ai9-hM3Dq model and pharmacological approach. DCZ activates hM3Dq in PVIs, potassium channels inactivate, and PKC is activated. MPEP and JNJ-16259685 block mGluR1 and mGluR5, which target PKC. PKC is antagonized with GF 109203X (GF). (**D**) DCZ rescues gamma potentiation in PV-Ai9-hM3Dq slices after blockade of mGluR1 and mGluR5. Left: Exemplary traces of control and DCZ conditions with and without MPEP and JNJ application. Corresponding PSDs below. Experiments performed in D-AP5 (50 μM) and DMSO (0.01%). Right: Barplot of average potentiation. (**E**) DCZ-dependent rescue requires PKC. Left: Traces and PSDs as in (D) for control and under application of GF. Experiments performed after preincubation (preinc.) with DMSO (0.01%) for 1 hour. Right: Barplot of average potentiation. Red insets ns in potentiation plots mark groups with no significant increase of peak gamma power in KA_2 ($P > 0.05$, Wilcoxon signed-rank test; power KA_2 versus KA_1). Numbers in plots denote n = number of slices tested for each group. ***$P < 0.001$ and ns (not significant), $P > 0.05$ (generalized linear model). Colored insets in PSDs and barplots highlight the application of DCZ.

to control experiments (Fig. 6D; power KA$_2$/KA$_1$ PV-Ai9-hM3Dq MPEP + JNJ + DCZ: 2.32 ± 0.21, n = 13). Third, gamma potentiation was alternatively prevented by preincubation with GF (3 μM, DMSO). In this case, co-application of DCZ failed to reinstate gamma potentiation (Fig. 6E; power KA$_2$/KA$_1$ PV-Ai9-hM3Dq control: 1.93 ± 0.12, n = 8 versus GF: 0.86 ± 0.11, n = 11 and GF + DCZ: 1.04 ± 0.05, n = 11). Therefore, gamma potentiation can be entirely accounted for by metabotropic signaling in PVIs dependent on a Gq/PKC- and a Gi-sensitive PKA pathway, with DREADD-based strategies in PVIs functioning as effective on/off switches for network plasticity.

DISCUSSION

Studying the intersections of interneuron plasticity, oscillatory activity, and learning has emerged as a challenging yet promising field of research (*40, 41*). Particularly in the hippocampus, the learning of context has been associated with changes of oscillation patterns: Following contextual fear conditioning in vivo, oscillations in the theta (*22*), gamma (*24*), and ripple (*22, 23*) frequency bands undergo plastic changes in CA1. In CA3, theta-gamma coupling increases during successive trials of item-context association (*5*), and low gamma power increases following object learning, a change associated with improved assembly formation of CA3 pyramidal cells (*7*). Whereas targeted cell-type–specific manipulations have linked some of these phenomena to the activation of interneurons, an understanding of cause and effect of oscillatory plasticity remains elusive. In a first step, we previously demonstrated that hippocampal gamma activity itself induces plasticity of sharp-wave ripple complexes in vivo and ex vivo, which was associated with synaptic plasticity on both pyramidal cells and interneurons (*29*).

Here, we present a general plasticity mechanism intrinsic to hippocampal network oscillations by which gamma power is increased upon repeated exposure to an equal excitatory stimulus (Fig. 1). This plasticity mechanism, gamma potentiation, is embedded in a reciprocal relationship with PVI synaptic plasticity (Figs. 4 to 6): Evoking network activity in the gamma frequency range induces long-lasting plasticity onto PVIs (*29, 35, 36, 42*), which, in turn, translates to subsequent network activity as a function of peak gamma power. Besides our PVI-specific interventions (Figs. 5 and 6), this is supported by two inductive approaches: Ex vivo, our data from CA1-Mini slices (fig. S3), a slice model of reduced recurrent excitation on pyramidal cells (*32*), demonstrate that local pyramidal cell–interneuron interactions are sufficient for the induction of oscillation plasticity. In silico, our microscale model of CA3 connectivity containing both PYR-PYR and PYR-PVI synapses further corroborates that plasticity at the PYR-PVI synapse critically outperforms plasticity at the PYR-PYR synapse in increasing low gamma power (Fig. 4). Intriguingly, PV-expressing interneurons themselves form diverse clusters of anatomically, molecularly, and physiologically distinct cell types (*43, 44*), which differentially contribute to network oscillations (*45*) and therefore may share or delegate contributions to their respective plasticity. Our modeling data assume a fast-spiking, basket cell–type morphology and predicts effective plasticity of gamma oscillations (Fig. 4). This is in line with findings demonstrating a heightened activity of fast-spiking, PV-expressing interneurons during gamma activity in vivo (*45*) and ex vivo (*46*). Once active, fast-spiking basket and axo-axonic cells exert powerful inhibition over the local pyramidal cell population,

e.g. during KA-evoked gamma oscillations (*18*), making them likely candidates for mediating gamma potentiation. However, we cannot exclude additional contributions of other interneuron subtypes: Dendrite-targeting, somatostatin (SOM)–positive interneurons substantially contribute to gamma oscillations in the hippocampus and neocortex (*47–50*). The transgenic lines used in this study are unlikely to target large populations of SOM-positive interneurons (*51*), yet coexpression of SOM and PV has been observed specifically in oriens–lacunosum moleculare (O-LM) interneurons, a cell-type particularly active during theta-nested gamma oscillations in vivo (*52*) and ex vivo (*53*). O-LM interneurons exhibit synaptic and intrinsic plasticity following theta-rate stimulation patterns that obey a similar profile as gamma plasticity, requiring CP-AMPARs and mGluR1 (*54*). Other than in PVIs, O-LM output is primarily modulated by theta rather than gamma oscillations (*45, 46*), making a direct overall contribution of O-LMs to gamma plasticity unlikely, yet predicting an indirect contribution via the modulation of concomitant theta states and/or in supporting long-range synchronization of gamma-coherent assemblies (*55*). In summary, our study provides a first step in identifying cell-type–specific cell-to-network plasticity of gamma oscillations and motivates more granular investigations of interneuron subtype-specific contributions. Within this study, and given our previous findings for gamma-induced plasticity (*29*), plasticity at the CA3 pyramidal cell–PV basket cell synapse is both sufficient and mandatory to modulate the gamma rhythm.

We investigate this relationship mechanistically using a robust (fig. S1) ex vivo paradigm, permitting the analysis of gamma activation states under maximal experimental control and circumventing confounders of in vivo oscillation power such as running speed, respiration rate, or cross-frequency coupling (*56, 57*), as well as spatial limitations concerning the origin (*6, 7, 58*) and focality (*59*) of oscillations. In the approach used here, gamma activity is gradually introduced to the isolated hippocampal network and tapered under constant control of external excitation via defined application of KA. This allows the precise mechanistic dissection of plasticity rules with pharmacological and genetic tools. Plasticity in our protocol occurs in an activity-dependent manner and already has effect after short- to intermediate-term delays in subsequent episodes (1 to 3 hours; fig. S2), predating alterations in transcriptional and anatomical PVI properties (*26, 27*) and making changes of transmembrane conductances the most likely mechanism. Although KA-induced ex vivo gamma power correlates with its in vivo counterpart and behavioral performance (*60*), our conclusions on plasticity remain to be confirmed in vivo. Translating our ex vivo model of gamma potentiation to the ground-truth in vivo gamma rhythm and possible effects on behavior will require temporally precise synapse-specific tools (*61*) and an experimental environment closely controlling the emergence and reinstatement of gamma oscillations on short timescales.

The specific synaptic recruitment of PVIs via CP-AMPARs is the decisive determinant in procuring and expressing gamma potentiation, as demonstrated by both our ex vivo and in silico data sets (Figs. 2 to 4). Through their rapid activation and decay kinetics, CP-AMPARs enable the temporally precise integration of converging inputs on and co-activation of PVIs (*62, 63*), which, as our data suggest, is mandatory for the induction of >30 Hz oscillations themselves. Therefore, increased CP-AMPAR conductance is a convincing mechanistic candidate underlying gamma potentiation. Given our previous findings for sharp-wave ripple–associated plasticity (*29*)

and present modeling predictions, this points to the induction of synaptic glutamatergic LTP onto PVIs (PVI-LTP) as the primary facilitator of gamma potentiation. The specific requirement of CP-AMPAR activation reported here separates our protocol from previous optogenetic or chemogenetic manipulations of network plasticity in vivo purportedly relying on the isolated activation of PVIs, but which cannot target or exclude coincident glutamatergic drive (22, 23, 64). Whether downstream effectors of PVI-LTP such as intrinsic membrane excitability (65) and/or an increased transmission at GABAergic output synapses (66–68) similarly contribute to the resulting field potential remains to be determined.

Like PVI-LTP in the dentate gyrus and gamma-mediated PVI-LTP in CA3 (29, 36), gamma potentiation is independent of NMDAR activation and instead requires group I mGluRs and downstream PKC, in line with a canonical Gq cascade. We tie this to PVIs with two genetic strategies: the conditional ablation of mGluR5 in PVIs and the PV-specific Gq-DREADD activation. Moreover, both our pharmacological and chemogenetic evidence using hM4Di activation suggest the requirement of a second pathway recruiting PKA (Figs. 5 and 6). A dual requirement of two kinase pathways may act as a gating mechanism for network plasticity (69): If gamma oscillations were both induced and amplified via CP-AMPAR activation alone, then local networks would be exposed to runoff dynamics in which oscillation power continuously increases. Expanding such a model by a prerequisite of metabotropic costimulation stabilizes network dynamics and discriminates between sub- and supra-critical stimuli to the hippocampal network during learning. This mirrors a recent proposal of three-factor plasticity in interneurons (41), in which mGluRs function as effective detectors of converging activity during oscillations (70), and putative activators of PKA (e.g., dopamine and noradrenaline) encode novelty (71, 72). Whether the Gq/PKC and PKA pathways effectuate plasticity independently, converge with each other, or interact via cross-talk (73) remains beyond the scope of this study yet may provide crucial insights into how targeting PVI-LTP translates into network oscillations.

The mechanistic composition of gamma potentiation provides a promising framework for the understanding and potential treatment of neuropsychiatric diseases associated with aberrant network oscillations. The PV-mGluR5 knockout model used here (Fig. 5) displays disrupted hippocampus-dependent behavior (34), establishing a direct link between insufficient ex vivo gamma plasticity and phenotypes of neurodevelopmental disease. mGluR5 activity is down-regulated in postmortem tissue of patients with schizophrenia (74), and, conversely, positive allosteric modulation of mGluR5 has been successfully targeted in animal models of schizophrenia (75), a disease etiologically tied to PVI dysfunction and disrupted network oscillations. The link between PVI plasticity, gamma potentiation, and disease is further supported by a string of recent preclinical studies successfully treating symptoms of neurodevelopmental disorders: Similar to the bimodal control of PVI-dependent DREADD manipulations over gamma potentiation (Fig. 6), hM4Di inhibition of PVIs induces deficits of cognitive performance (23, 76), while PVI-specific hM3Dq activation rescues such deficits in animal models of schizophrenia and disruptions in network oscillations (76–78). Further, the physiological induction of gamma oscillations via sensory stimuli (gamma entrainment using sensory stimuli) is itself effective in treating animals models of Alzheimer's disease (79) and schizophrenia (80), whereas the exact mechanism underlying these treatments has been recently contested (81). An inert, bidirectional cortical mechanism of gamma rhythm plasticity via synaptic plasticity of PVIs may therefore lie at the core of future clinical interventions and serve to inform therapeutic strategies.

MATERIALS AND METHODS
Animals
Adolescent (P45 to P70) male C57Bl6/J mice (the Jackson Laboratory, RRID:IMSR_JAX:000664) were used for experiments in WT animals. For experiments involving cell-type–specific manipulations of PVIs, PV-Cre animals (the Jackson Laboratory, RRID:IMSR_JAX:017320) were crossbred with either Ai9 (the Jackson Laboratory, RRID:IMSR_JAX:007909), loxp-mG5 (RRID:IMSR_JAX:028626, provided by P. Wulff), Flex-hM4Di [Rosa26-FLEX-hM4D (MGI:7528984); see (37); provided by B. Rost], or loxp-hM3Dq (the Jackson Laboratory, RRID:IMSR_JAX:026220) animals, and experiments were performed from adolescent (P45 to P70) offspring of both sexes. Animal procedures were conducted in accordance with the guidelines of the European Communities Council and the institutional guidelines approved by the Berlin Animal Ethics Committee (Landesamt für Gesundheit und Soziales Berlin, T0045/15 and T-CH0014/23). All efforts were made to minimize animal suffering and to reduce the number of animals used.

Slice preparation
Mice were deeply anesthetized with isoflurane and decapitated. Their brains were removed and immersed in ice-cold sucrose solution (75 mM sucrose, 87 mM NaCl, 2.5 mM KCl, 25 mM NaHCO$_3$, 1.25 mM NaH$_2$PO$_4$, 3 mM MgCl$_2$, 0.5 mM CaCl$_2$, and 10 mM glucose) saturated with carbogen gas (95% O$_2$/5% CO$_2$). The brain was cut into 400-μm-thick horizontal slices containing the hippocampal formation with a vibratome (Leica VT 1200S, Leica Biosystems, Germany). Slices were subsequently transferred to interface-type recording chambers perfused with ACSF (129 mM NaCl, 3 mM KCl, 21 mM NaHCO$_3$, 1.25 mM NaH$_2$PO$_4$, 1.8 mM MgSO$_4$, 1.6 mM CaCl$_2$, and 10 mM glucose; 32° to 34°C; flow rate, 1.5 ml/min) saturated with carbogen and left to incubate for 2 hours before recordings. To obtain CA1-Mini slices, slices were cut in the interface chamber shortly after preparation with a surgical blade to separate CA1 from CA2 and the subiculum under consideration of CA1 dendrite morphology.

For experiments involving pharmacological agents, drugs were added to the ACSF at least 1 hour before recording. In experiments involving GF or H-89, slices were first left to recover for 1 hour after slicing in a submerged-type beaker at 34°C containing the respective substance diluted at its final concentration in sucrose solution before being transferred to interface chambers. Corresponding control experiments were performed in the presence of 0.01% DMSO in the beaker.

Electrophysiology
LFP recordings
LFPs were recorded from stratum pyramidale of hippocampal CA3 (and/or CA1 when indicated) with glass pipettes filled with ACSF (1 to 10 megaohms). Recordings were amplified by EXB-EXT-02B amplifiers (npi Electronic, Germany), low-pass–filtered at 1 kHz, sampled at 5 kHz by a CED 1401 AD-converter [Cambridge Electronic

Design (CED), UK] and saved to disk via Spike2 software (CED, UK, RRID:SCR_000903). Following an initial 30-min period of recording baseline activity, network oscillations were induced in one or two separate periods by bath application of 150 to 400 nM KA over a period of 30 min with a 60-min "resting" interval between both application periods. In a subset of experiments, the resting period was extended to 3 hours. After the second application of KA, slices rested for up to 1 hour before terminating the recording. Pipette resistances were monitored before and after recordings with an EXB-REL08B electrode resistance meter (npi), and recordings were discarded if resistances deviated >10%.

pMEA recordings
pMEA recordings were performed on a MEA2100-HS(2x)60 system (Multichannel Systems) using 60pMEA100/30iR-Ti pMEAs (Multichannel Systems). Slices were transferred from their previous interface storage to the pMEA and carefully placed above the electrodes with the aim of maximal coverage of the pyramidal cell layer (identified visually under magnification and confirmed by the positive polarity of spontaneous sharp-wave ripple complexes). Slices were kept in place via a continuous negative pressure supplied by a constant vacuum pump (CVP-230 V, Multichannel Systems) and allowed to rest in position for 15 to 20 min before recording. After a brief recording of baseline activity confirming the absence of ambient gamma oscillations, oscillations were induced via bath application of 200 nM KA (flow rate of 10 ml/min, 32° to 34°C). The dual headstage configuration of the MEA2100-HS(2x)60 system allowed us to test individual treated and untreated slices in time control.

Drugs
KA (Tocris), D-AP5 (Cayman Chemicals), MPEP (Cayman Chemicals), JNJ-16259685 (Tocris, JNJ), GYKI-53655 (hellobio), NASPM (Cayman Chemicals, NASPM), GF(Tocris), H-89 (Cayman Chemicals), UBP-302 (Tocris, UBP), DCZ-dihydrochloride (Cayman Chemicals), nifedipine (Tocris), and ML-218 (Tocris) were dissolved in either deionized water or DMSO (JNJ, GF, H-89, UBP, nifedipine, and ML-218) and stored in aliquots at −20°C. Aliquots were dissolved in ACSF immediately before the experiments. Experiments involving nifedipine were conducted in the dark.

Computational modeling
Model implementation and availability
We conducted all modeling simulations using the NEURON (NEURON v7.6, RRID:SCR_005393) Simulator (82) on a High-Performance Computing Cluster with 111 CPU cores, running on a 64-bit CentOS Linux operating system. The source code and datasets used to generate Fig. 4 are publicly available; please refer to the Data and materials availability statement for the link.

PV basket cell model
The multi-compartmental models of the CA3 PV basket cells (PVIs) ($n = 2$) used in this study were adapted from previously published work (33). These models have been extensively validated against experimental data and have been shown to accurately capture the intrinsic, active, and morphological properties of PVIs (for more detailed information, please refer to the previous publication).

Pyramidal neuron model
The CA3 pyramidal neuron cell model (PYR) was simulated on the basis of the Hodgkin-Huxley formalism and consists of six compartments: one soma and five dendrites. The model simulates one proximal and two distal apical dendrites, as well as two basal

dendrites. It includes a Ca^{2+} pump and buffering mechanism, Ca^{2+}-activated slow AHP and medium AHP potassium (K^+) currents, an HVA L-type calcium (Ca^{2+}) current, an HVA R-type Ca^{2+} current, an LVA T-type Ca^{2+} current, an h current, a fast sodium (Na^+) current, a delayed rectifier K^+ current, a slowly inactivating K^+ M-type current, and a fast inactivating K^+ A-type current. The current mechanisms were distributed in a nonuniform way along the somatodendritic compartments (for detailed information about the passive and active properties of the PYR model, including conductance values, please see table S1). The active and passive properties of the PYR model were validated against in vitro experimental data from CA3 recordings (83). This was done to ensure that the in silico model reproduces the electrophysiological profile of the in vitro CA3 pyramidal cells (for more detailed information, please see table S2).

Synaptic properties
The PYR models were equipped with CI-AMPA, NMDA, and γ-aminobutyric acid type A ($GABA_A$) synapses, while the PV BC models had CP-AMPA, NMDA, $GABA_A$, and autaptic $GABA_A$ synapses. The synaptic properties were validated against previously published data (84–86). The conductance values for each synapse type are provided in table S3.

Plasticity protocols
The plasticity simulations were performed by increasing the conductance values of different types of synapses in the microcircuit model. Specifically, the three conditions tested were PYR plasticity (PYR-LTP), which involved a 50% increase in the CI-AMPA conductance value of PYR to PYR connections, PVI plasticity (PVI-LTP), which involved a 50% increase in the CP-AMPA conductance value of PYR to PVI connections, and PYR and PVI plasticity (PYR + PVI-LTP), which involved a 50% increase in both the CI-AMPA and CP-AMPA conductance values of PYR to PYR and PYR to PVI connections (see also table S3).

Microcircuit configuration
The biologically constrained CA3 microcircuit model comprised 22 neurons, specifically 20 PYRs and 2 PVIs. In each random simulation trial ($n = 10$), each PYR contacted up to four other PYRs with one CI-AMPA and one NMDA synapse activation per contact (convergence = 1). On the other hand, every PVI received synaptic input (convergence = 1) from five different PYRs in each simulation trial. In addition, every PYR received one feedback inhibitory GABAergic input from each PVI per simulation trial. Each of the two PVIs formed four GABAergic synapses per simulation trial and was self-inhibited through autapses. To record the LFP, an in silico electrode was simulated on the basis of NEURON's extracellular function [based on (87)]. The electrode was placed close to the PYR somata and remained in the same position throughout the simulation trials. The sampling frequency was set at 10 kHz. For simplicity reasons, other inhibitory interneuron types, such as dendrite-targeting interneurons, and network properties, such as gap junctions, were not simulated as they were not relevant to the experimental observations of this study.

Inputs and simulation
The input was modeled as an artificial presynaptic population using NEURON's NetStim function (interval = 30, number = 30). The input targeted only the PYR population of the microcircuit for 1 s, and three input synapses were activated in every pyramidal cell (see table S3), mimicking the experimental protocol of KA activation primarily in the pyramidal cells. In addition, both pyramidal cells

and PVI populations received the same excitatory subthreshold background fluctuation input (subthreshold noise). For every case (including baseline, PYR-LTP, PVI-LTP, or PYR + PVI-LTP), we ran the microcircuit for 10 random trials. In every trial, the number of total synaptic contacts and the connectivity ratios remained identical, but different random neurons were connected to different random neurons. To capture any variability related to morphological features, synapses were allocated in different random dendrites and locations across the selected dendrites in every trial. The recording time was 2 s for every simulation trial.

Data analysis and statistics
LFP recordings
Recordings were band-pass–filtered (1 to 100 Hz, 12 pole IIR digital filter) and band-stop–filtered (49 to 51 Hz, 12 pole IIR digital filter). Power spectra were calculated every 30 s throughout the recording in each recorded slice individually. Peak power and peak frequency were determined offline by using custom-made MATLAB scripts and visualized as time-power and time-frequency plots, respectively. Slices were excluded from analysis if (i) they only displayed synchronous activity for an interval shorter than 10 min or during only one induction period or (ii) network activity was instable, e.g., peak power would intermittently decrease during KA application by >10%.

For each included slice, a 10-min time window was detected corresponding to maximal peak power in the first induction period. Peak power and frequency were extracted from an additional 10-min power spectral density obtained with MATLABs "pwelch" function (0.34-Hz resolution) and auto-/cross-correlograms obtained over the same interval with the "xcorr" function. For experiments investigating network activity in two separate episodes of KA application, the identical analysis was performed twice in time control to the first application period.

pMEA recordings
Recordings were preprocessed, and peak power and frequency values as well as cross-correlograms for each channel were obtained identically to LFP recordings. Channels included in subsequent analysis were identified by their positioning below the pyramidal cell layer, marked as nodes in relation to their position on the pMEA that were connected via edges to the respectively adjacent selected electrodes (MATLAB "digraph" function). For each individual recording, a lead electrode, corresponding to the highest peak power value determined, was identified. Intralaminar distances to this electrode were calculated with the "shortestpath" MATLAB function.

Simulation data
Data were band-pass– and band-stop–filtered as LFP recordings. Power spectra were obtained from the entire 2-s recording with the same parameters as LFP recordings and peak power values extracted between 20 and 40 Hz.

Statistical analysis
Statistical analysis and data visualization were performed in R 4.1.3. As absolute peak spectral power is non-normally distributed in our datasets and in single LFP recordings is highly dependent on the intralaminar location of the recording site (compare Fig. 3 and fig. S4), all testing on raw power data was performed nonparametrically using the Mann-Whitney U test (independent samples) or Wilcoxon signed-rank test (dependent samples). Power data are presented as median [first quartile, third quartile] and visualized as boxplots (crosses in boxplots denote the mean). Other positive-only,

skewed datasets (i.e., peak frequency of network oscillations or potentiation of peak power; compare fig. S1) were fitted with a generalized linear model assuming a log-linked gamma distribution (*88*) to account for zero truncation. T statistics and P values for group comparisons were subsequently obtained from the estimated marginal means ("emmeans" package, https://cran.r-project.org/web/packages/emmeans/index.html). Non-power data are presented as means ± SEM and visualized as barplots. Numbers in barplots or below boxplots denote the sample size with n referring to the number of slices tested or simulation trials run, respectively. Significance was set to an α level of 0.05. P values obtained from multiple group comparisons were corrected with the Bonferroni-Holm method.

Supplementary Materials
This PDF file includes:
Figs. S1 to S8
Tables S1 to S3

REFERENCES AND NOTES
1. W. Singer, Neuronal oscillations: Unavoidable and useful? *Eur. J. Neurosci.* **48**, 2389–2398 (2018).
2. Z. Nadasdy, D. H. P. Howell, A. Török, T. P. Nguyen, J. Y. Shen, D. E. Briggs, P. N. Modur, R. J. Buchanan, Phase coding of spatial representations in the human entorhinal cortex. *Sci. Adv.* **8**, eabm6081 (2022).
3. G. Buzsáki, A. Draguhn, Neuronal oscillations in cortical networks. *Science* **304**, 1926–1929 (2004).
4. G. Buzsáki, *Rhythms of the Brain* (Oxford Univ. Press, 2006).
5. A. B. L. Tort, R. W. Komorowski, J. R. Manns, N. J. Kopell, H. Eichenbaum, Theta–gamma coupling increases during the learning of item–context associations. *Proc. Natl. Acad. Sci. U.S.A.* **106**, 20942–20947 (2009).
6. V. Lopes-dos-Santos, G. M. van de Ven, A. Morley, S. Trouche, N. Campo-Urriza, D. Dupret, Parsing hippocampal theta oscillations by nested spectral components during spatial exploration and memory-guided behavior. *Neuron* **100**, 940–952.e7 (2018).
7. A. Fernández-Ruiz, A. Oliva, M. Soula, F. Rocha-Almeida, G. A. Nagy, G. Martin-Vazquez, G. Buzsáki, Gamma rhythm communication between entorhinal cortex and dentate gyrus neuronal assemblies. *Science* **372**, eabf3119 (2021).
8. P. J. Uhlhaas, W. Singer, Neural synchrony in brain disorders: Relevance for cognitive dysfunctions and pathophysiology. *Neuron* **52**, 155–168 (2006).
9. J. A. Cardin, M. Carlén, K. Meletis, U. Knoblich, F. Zhang, K. Deisseroth, L.-H. Tsai, C. I. Moore, Driving fast-spiking cells induces gamma rhythm and controls sensory responses. *Nature* **459**, 663–667 (2009).
10. V. S. Sohal, F. Zhang, O. Yizhar, K. Deisseroth, Parvalbumin neurons and gamma rhythms enhance cortical circuit performance. *Nature* **459**, 698–702 (2009).
11. K. K. A. Cho, R. Hoch, A. T. Lee, T. Patel, J. L. R. Rubenstein, V. S. Sohal, Gamma rhythms link prefrontal interneuron dysfunction with cognitive inflexibility in Dlx5/6$^{+/−}$ mice. *Neuron* **85**, 1332–1343 (2015).
12. G. Buzsáki, X.-J. Wang, Mechanisms of gamma oscillations. *Annu. Rev. Neurosci.* **35**, 203–225 (2012).
13. L. L. Colgin, Rhythms of the hippocampal network. *Nat. Rev. Neurosci.* **17**, 239–249 (2016).
14. M. Bartos, I. Vida, P. Jonas, Synaptic mechanisms of synchronized gamma oscillations in inhibitory interneuron networks. *Nat. Rev. Neurosci.* **8**, 45–56 (2007).
15. X.-J. Wang, G. Buzsáki, Gamma oscillation by synaptic inhibition in a hippocampal interneuronal network model. *J. Neurosci.* **16**, 6402–6413 (1996).
16. E. O. Mann, J. M. Suckling, N. Hajos, S. A. Greenfield, O. Paulsen, Perisomatic feedback inhibition underlies cholinergically induced fast network oscillations in the rat hippocampus in vitro. *Neuron* **45**, 105–117 (2005).
17. B. V. Atallah, M. Scanziani, Instantaneous modulation of gamma oscillation frequency by balancing excitation with inhibition. *Neuron* **62**, 566–577 (2009).
18. T. Dugladze, D. Schmitz, M. A. Whittington, I. Vida, T. Gloveli, Segregation of axonal and somatic activity during fast network oscillations. *Science* **336**, 1458–1461 (2012).
19. H. Hu, J. Gan, P. Jonas, Fast-spiking, parvalbumin GABAergic interneurons: From cellular design to microcircuit function. *Science* **345**, 1255263 (2014).
20. E. C. Fuchs, H. Doheny, H. Faulkner, A. Caputi, R. D. Traub, A. Bibbig, N. Kopell, M. A. Whittington, H. Monyer, Genetically altered AMPA-type glutamate receptor kinetics in interneurons disrupt long-range synchrony of gamma oscillation. *Proc. Natl. Acad. Sci. U.S.A.* **98**, 3571–3576 (2001).

21. E. C. Fuchs, A. R. Zivkovic, M. O. Cunningham, S. Middleton, F. E. N. LeBeau, D. M. Bannerman, A. Rozov, M. A. Whittington, R. D. Traub, J. N. P. Rawlins, H. Monyer, Recruitment of parvalbumin-positive interneurons determines hippocampal function and associated behavior. *Neuron* **53**, 591–604 (2007).

22. N. Ognjanovski, S. Schaeffer, J. Wu, S. Mofakham, D. Maruyama, M. Zochowski, S. J. Aton, Parvalbumin-expressing interneurons coordinate hippocampal network dynamics required for memory consolidation. *Nat. Commun.* **8**, 15039 (2017).

23. F. Xia, B. A. Richards, M. M. Tran, S. A. Josselyn, K. Takehara-Nishiuchi, P. W. Frankland, Parvalbumin-positive interneurons mediate neocortical-hippocampal interactions that are necessary for memory consolidation. *eLife* **6**, e27868 (2017).

24. X. He, J. Li, G. Zhou, J. Yang, S. McKenzie, Y. Li, W. Li, J. Yu, Y. Wang, J. Qu, Z. Wu, H. Hu, S. Duan, H. Ma, Gating of hippocampal rhythms and memory by synaptic plasticity in inhibitory interneurons. *Neuron* **109**, 1013–1028.e9 (2021).

25. A. I. Ramsaran, Y. Wang, A. Golbabaei, S. Aleshin, M. L. de Snoo, B. A. Yeung, A. J. Rashid, A. Awasthi, J. Lau, L. M. Tran, S. Y. Ko, A. Abegg, L. C. Duan, C. McKenzie, J. Gallucci, M. Ahmed, R. Kaushik, A. Dityatev, S. A. Josselyn, P. W. Frankland, A shift in the mechanisms controlling hippocampal engram formation during brain maturation. *Science* **380**, 543–551 (2023).

26. F. Donato, S. B. Rompani, P. Caroni, Parvalbumin-expressing basket-cell network plasticity induced by experience regulates adult learning. *Nature* **504**, 272–276 (2013).

27. N. Dehorter, G. Ciceri, G. Bartolini, L. Lim, I. del Pino, O. Marín, Tuning of fast-spiking interneuron properties by an activity-dependent transcriptional switch. *Science* **349**, 1216–1220 (2015).

28. D. M. Kullmann, K. P. Lamsa, Long-term synaptic plasticity in hippocampal interneurons. *Nat. Rev. Neurosci.* **8**, 687–699 (2007).

29. S. Zarnadze, P. Bäuerle, J. Santos-Torres, C. Böhm, D. Schmitz, J. R. Geiger, T. Dugladze, T. Gloveli, Cell-specific synaptic plasticity induced by network oscillations. *eLife* **5**, e14912 (2016).

30. R. Zemankovics, J. M. Veres, I. Oren, N. Hájos, Feedforward inhibition underlies the propagation of cholinergically induced gamma oscillations from hippocampal CA3 to CA1. *J. Neurosci.* **33**, 12337–12351 (2013).

31. R. D. Traub, M. O. Cunningham, T. Gloveli, F. E. N. LeBeau, A. Bibbig, E. H. Buhl, M. A. Whittington, GABA-enhanced collective behavior in neuronal axons underlies persistent gamma-frequency oscillations. *Proc. Natl. Acad. Sci. U.S.A.* **100**, 11047–11052 (2003).

32. S. Yang, S. Yang, T. Moreira, G. Hoffman, G. C. Carlson, K. J. Bender, B. E. Alger, C.-M. Tang, Interlamellar CA1 network in the hippocampus. *Proc. Natl. Acad. Sci. U.S.A.* **111**, 12919–12924 (2014).

33. A. Tzilivaki, G. Kastellakis, P. Poirazi, Challenging the point neuron dogma: FS basket cells as 2-stage nonlinear integrators. *Nat. Commun.* **10**, 3664 (2019).

34. S. A. Barnes, A. Pinto-Duarte, A. Kappe, A. Zembrzycki, A. Metzler, E. A. Mukamel, J. Lucero, X. Wang, T. J. Sejnowski, A. Markou, M. M. Behrens, Disruption of mGluR5 in parvalbumin-positive interneurons induces core features of neurodevelopmental disorders. *Mol. Psychiatry* **20**, 1161–1172 (2015).

35. K. P. Lamsa, J. H. Heeroma, P. Somogyi, D. A. Rusakov, D. M. Kullmann, Anti-Hebbian long-term potentiation in the hippocampal feedback inhibitory circuit. *Science* **315**, 1262–1266 (2007).

36. T. Hainmuller, K. Krieglstein, A. Kulik, M. Bartos, Joint CP-AMPA and group I mGlu receptor activation is required for synaptic plasticity in dentate gyrus fast-spiking interneurons. *Proc. Natl. Acad. Sci. U.S.A.* **111**, 13211–13216 (2014).

37. R. De Filippo, B. R. Rost, A. Stumpf, C. Cooper, J. J. Tukker, C. Harms, P. Beed, D. Schmitz, Somatostatin interneurons activated by 5-HT2A receptor suppress slow oscillations in medial entorhinal cortex. *eLife* **10**, e66960 (2021).

38. Y. Nagai, N. Miyakawa, H. Takuwa, Y. Hori, K. Oyama, B. Ji, M. Takahashi, X.-P. Huang, S. T. Slocum, J. F. DiBerto, Y. Xiong, T. Urushihata, T. Hirabayashi, A. Fujimoto, K. Mimura, J. G. English, J. Liu, K. Inoue, K. Kumata, C. Seki, M. Ono, M. Shimojo, M.-R. Zhang, Y. Tomita, J. Nakahara, T. Suhara, M. Takada, M. Higuchi, J. Jin, B. L. Roth, T. Minamimoto, Deschloroclozapine, a potent and selective chemogenetic actuator enables rapid neuronal and behavioral modulations in mice and monkeys. *Nat. Neurosci.* **23**, 1157–1167 (2020).

39. D. Atasoy, S. M. Sternson, Chemogenetic tools for causal cellular and neuronal biology. *Physiol. Rev.* **98**, 391–418 (2018).

40. L. Topolnik, S. Tamboli, The role of inhibitory circuits in hippocampal memory processing. *Nat. Rev. Neurosci.* **23**, 476–492 (2022).

41. A. R. McFarlan, C. Y. C. Chou, A. Watanabe, N. Cherepacha, M. Haddad, H. Owens, P. J. Sjöström, The plasticitome of cortical interneurons. *Nat. Rev. Neurosci.* **24**, 80–97 (2022).

42. H. Alle, P. Jonas, J. R. P. Geiger, PTP and LTP at a hippocampal mossy fiber-interneuron synapse. *Proc. Natl. Acad. Sci. U.S.A.* **98**, 14708–14713 (2001).

43. R. D. Hodge, T. E. Bakken, J. A. Miller, K. A. Smith, E. R. Barkan, L. T. Graybuck, J. L. Close, B. Long, N. Johansen, O. Penn, Z. Yao, J. Eggermont, T. Höllt, B. P. Levi, S. I. Shehata, B. Aevermann, A. Beller, D. Bertagnolli, K. Brouner, T. Casper, C. Cobbs, R. Dalley, N. Dee, S.-L. Ding, R. G. Ellenbogen, O. Fong, E. Garren, J. Goldy, R. P. Gwinn, D. Hirschstein, C. D. Keene, M. Keshk, A. L. Ko, K. Lathia, A. Mahfouz, Z. Maltzer, M. McGraw, T. N. Nguyen, J. Nyhus, J. G. Ojemann, A. Oldre, S. Parry, S. Reynolds, C. Rimorin, N. V. Shapovalova, S. Somasundaram, A. Szafer, E. R. Thomsen, M. Tieu, G. Quon, R. H. Scheuermann, R. Yuste, S. M. Sunkin, B. Lelieveldt, D. Feng, L. Ng, A. Bernard, M. Hawrylycz, J. W. Phillips, B. Tasic, H. Zeng, A. R. Jones, C. Koch, E. S. Lein, Conserved cell types with divergent features in human versus mouse cortex. *Nature* **573**, 61–68 (2019).

44. S. Bugeon, J. Duffield, M. Dipoppa, A. Ritoux, I. Prankerd, D. Nicoloutsopoulos, D. Orme, M. Shinn, H. Peng, H. Forrest, A. Viduolyte, C. B. Reddy, Y. Isogai, M. Carandini, K. D. Harris, A transcriptomic axis predicts state modulation of cortical interneurons. *Nature* **607**, 330–338 (2022).

45. T. Klausberger, P. Somogyi, Neuronal diversity and temporal dynamics: The unity of Hippocampal circuit operations. *Science* **321**, 53–57 (2008).

46. T. Gloveli, T. Dugladze, S. Saha, H. Monyer, U. Heinemann, R. D. Traub, M. A. Whittington, E. H. Buhl, Differential involvement of oriens/pyramidale interneurones in hippocampal network oscillationsin vitro. *J. Physiol.* **562**, 131–147 (2005).

47. P. Antonoudiou, Y. L. Tan, G. Kontou, A. L. Upton, E. O. Mann, Parvalbumin and somatostatin interneurons contribute to the generation of Hippocampal gamma oscillations. *J. Neurosci.* **40**, 7668–7687 (2020).

48. J. Veit, R. Hakim, M. P. Jadi, T. J. Sejnowski, H. Adesnik, Cortical gamma band synchronization through somatostatin interneurons. *Nat. Neurosci.* **20**, 951–959 (2017).

49. L. Liu, H. Xu, J. Wang, J. Li, Y. Tian, J. Zheng, M. He, T.-L. Xu, Z.-Y. Wu, X.-M. Li, S.-M. Duan, H. Xu, Cell type–differential modulation of prefrontal cortical GABAergic interneurons on low gamma rhythm and social interaction. *Sci. Adv.* **6**, eaay4073 (2020).

50. J. Veit, G. Handy, D. P. Mossing, B. Doiron, H. Adesnik, Cortical VIP neurons locally control the gain but globally control the coherence of gamma band rhythms. *Neuron* **111**, 405–417.e5 (2023).

51. L. Que, D. Lukacsovich, W. Luo, C. Földy, Transcriptional and morphological profiling of parvalbumin interneuron subpopulations in the mouse hippocampus. *Nat. Commun.* **12**, 108 (2021).

52. J. J. Tukker, P. Fuentealba, K. Hartwich, P. Somogyi, T. Klausberger, Cell type-specific tuning of hippocampal interneuron firing during gamma oscillations *in vivo*. *J. Neurosci.* **27**, 8184–8189 (2007).

53. T. Gloveli, T. Dugladze, H. G. Rotstein, R. D. Traub, H. Monyer, U. Heinemann, M. A. Whittington, N. J. Kopell, Orthogonal arrangement of rhythm-generating microcircuits in the hippocampus. *Proc. Natl. Acad. Sci. U.S.A.* **102**, 13295–13300 (2005).

54. M. Sammari, Y. Inglebert, N. Ankri, M. Russier, S. Incontro, D. Debanne, Theta patterns of stimulation induce synaptic and intrinsic potentiation in O-LM interneurons. *Proc. Natl. Acad. Sci. U.S.A.* **119**, e2205264119 (2022).

55. A. B. L. Tort, H. G. Rotstein, T. Dugladze, T. Gloveli, N. J. Kopell, On the formation of gamma-coherent cell assemblies by oriens lacunosum-moleculare interneurons in the hippocampus. *Proc. Natl. Acad. Sci. U.S.A.* **104**, 13490–13495 (2007).

56. C. Zheng, K. W. Bieri, S. G. Trettel, L. L. Colgin, The relationship between gamma frequency and running speed differs for slow and fast gamma rhythms in freely behaving rats. *Hippocampus* **25**, 924–938 (2015).

57. W. Zhong, M. Ciatipis, T. Wolfenstetter, J. Jessberger, C. Müller, S. Ponsel, Y. Yanovsky, J. Brankačk, A. B. L. Tort, A. Draguhn, Selective entrainment of gamma subbands by different slow network oscillations. *Proc. Natl. Acad. Sci. U.S.A.* **114**, 4519–4524 (2017).

58. B. Lasztóczi, T. Klausberger, Hippocampal place cells couple to three different gamma oscillations during place field traversal. *Neuron* **91**, 34–40 (2016).

59. M. Strüber, J.-F. Sauer, P. Jonas, M. Bartos, Distance-dependent inhibition facilitates focality of gamma oscillations in the dentate gyrus. *Nat. Commun.* **8**, 758 (2017).

60. C. B. Lu, J. G. R. Jefferys, E. C. Toescu, M. Vreugdenhil, In vitro hippocampal gamma oscillation power as an index of in vivo CA3 gamma oscillation strength and spatial reference memory. *Neurobiol. Learn. Mem.* **95**, 221–230 (2011).

61. B. R. Rost, J. Wietek, O. Yizhar, D. Schmitz, Optogenetics at the presynapse. *Nat. Neurosci.* **25**, 984–998 (2022).

62. J. R. P. Geiger, T. Melcher, D.-S. Koh, B. Sakmann, P. H. Seeburg, P. Jonas, H. Monyer, Relative abundance of subunit mRNAs determines gating and Ca^{2+} permeability of AMPA receptors in principal neurons and interneurons in rat CNS. *Neuron* **15**, 193–204 (1995).

63. J. R. P. Geiger, J. Lübke, A. Roth, M. Frotscher, P. Jonas, Submillisecond AMPA receptor-mediated signaling at a principal neuron–interneuron synapse. *Neuron* **18**, 1009–1023 (1997).

64. G. Etter, S. van der Veldt, F. Manseau, I. Zarrinkoub, E. Trillaud-Doppia, S. Williams, Optogenetic gamma stimulation rescues memory impairments in an Alzheimer's disease mouse model. *Nat. Commun.* **10**, 5322 (2019).

65. E. Campanac, C. Gasselin, A. Baude, S. Rama, N. Ankri, D. Debanne, Enhanced intrinsic excitability in basket cells maintains excitatory-inhibitory balance in hippocampal circuits. *Neuron* **77**, 712–722 (2013).

66. M. Udakis, V. Pedrosa, S. E. L. Chamberlain, C. Clopath, J. R. Mellor, Interneuron-specific plasticity at parvalbumin and somatostatin inhibitory synapses onto CA1 pyramidal neurons shapes hippocampal output. *Nat. Commun.* **11**, 4395 (2020).

67. E. D. Vickers, C. Clark, D. Osypenko, A. Fratzl, O. Kochubey, B. Bettler, R. Schneggenburger, Parvalbumin-interneuron output synapses show spike-timing-dependent plasticity that contributes to auditory map remodeling. *Neuron* **99**, 720–735.e6 (2018).

68. E.-L. Yap, N. L. Pettit, C. P. Davis, M. A. Nagy, D. A. Harmin, E. Golden, O. Dagliyan, C. Lin, S. Rudolph, N. Sharma, E. C. Griffith, C. D. Harvey, M. E. Greenberg, Bidirectional perisomatic inhibitory plasticity of a Fos neuronal network. *Nature* **590**, 115–121 (2021).

69. Z. Brzosko, S. B. Mierau, O. Paulsen, Neuromodulation of spike-timing-dependent plasticity: Past, present, and future. *Neuron* **103**, 563–581 (2019).

70. A. Reiner, J. Levitz, Glutamatergic signaling in the central nervous system: Ionotropic and metabotropic receptors in concert. *Neuron* **98**, 1080–1098 (2018).

71. A. Wagatsuma, T. Okuyama, C. Sun, L. M. Smith, K. Abe, S. Tonegawa, Locus coeruleus input to hippocampal CA3 drives single-trial learning of a novel context. *Proc. Natl. Acad. Sci. U.S.A.* **115**, E310–E316 (2018).

72. A. Chowdhury, A. Luchetti, G. Fernandes, D. A. Filho, G. Kastellakis, A. Tzilivaki, E. M. Ramirez, M. Y. Tran, P. Poirazi, A. J. Silva, A locus coeruleus-dorsal CA1 dopaminergic circuit modulates memory linking. *Neuron* **110**, 3374–3388.E8 (2022).

73. Y. Chen, A. J. Granger, T. Tran, J. L. Saulnier, A. Kirkwood, B. L. Sabatini, Endogenous Gαq-coupled neuromodulator receptors activate protein kinase a. *Neuron* **96**, 1070–1083.e5 (2017).

74. H.-Y. Wang, M. L. MacDonald, K. E. Borgmann-Winter, A. Banerjee, P. Sleiman, A. Tom, A. Khan, K.-C. Lee, P. Roussos, S. J. Siegel, S. E. Hemby, W. B. Bilker, R. E. Gur, C.-G. Hahn, mGluR5 hypofunction is integral to glutamatergic dysregulation in schizophrenia. *Mol. Psychiatry* **25**, 750–760 (2020).

75. J. M. Rook, Z. Xiang, X. Lv, A. Ghoshal, J. W. Dickerson, T. M. Bridges, K. A. Johnson, D. J. Foster, K. J. Gregory, P. N. Vinson, A. D. Thompson, N. Byun, R. L. Collier, M. Bubser, M. T. Nedelcovych, R. W. Gould, S. R. Stauffer, J. S. Daniels, C. M. Niswender, H. Lavreysen, C. Mackie, S. Conde-Ceide, J. Alcazar, J. M. Bartolomé-Nebreda, G. J. Macdonald, J. C. Talpos, T. Steckler, C. K. Jones, C. W. Lindsley, P. J. Conn, Biased mGlu 5-positive allosteric modulators provide in vivo efficacy without potentiating mGlu 5 modulation of NMDAR currents. *Neuron* **86**, 1029–1040 (2015).

76. Y. Huang, H. Jiang, Q. Zheng, A. H. K. Fok, X. Li, C. G. Lau, C. S. W. Lai, Environmental enrichment or selective activation of parvalbumin-expressing interneurons ameliorates synaptic and behavioral deficits in animal models with schizophrenia-like behaviors during adolescence. *Mol. Psychiatry* **26**, 2533–2552 (2021).

77. A. Mukherjee, F. Carvalho, S. Eliez, P. Caroni, Long-lasting rescue of network and cognitive dysfunction in a genetic Schizophrenia model. *Cell* **178**, 1387–1402.e14 (2019).

78. T. Marissal, R. F. Salazar, C. Bertollini, S. Mutel, M. De Roo, I. Rodriguez, D. Müller, A. Carleton, Restoring wild-type-like CA1 network dynamics and behavior during adulthood in a mouse model of schizophrenia. *Nat. Neurosci.* **21**, 1412–1420 (2018).

79. C. Adaikkan, S. J. Middleton, A. Marco, P.-C. Pao, H. Mathys, D. N.-W. Kim, F. Gao, J. Z. Young, H.-J. Suk, E. S. Boyden, T. J. McHugh, L.-H. Tsai, Gamma entrainment binds higher-order brain regions and offers neuroprotection. *Neuron* **102**, 929–943.e8 (2019).

80. M. Shen, Y. Guo, Q. Dong, Y. Gao, M. E. Stockton, M. Li, S. Kannan, T. Korabelnikov, K. A. Schoeller, C. L. Sirois, C. Zhou, J. Le, D. Wang, Q. Chang, Q.-Q. Sun, X. Zhao, FXR1 regulation of parvalbumin interneurons in the prefrontal cortex is critical for schizophrenia-like behaviors. *Mol. Psychiatry* **26**, 6845–6867 (2021).

81. M. Soula, A. Martín-Ávila, Y. Zhang, A. Dhingra, N. Nitzan, M. J. Sadowski, W.-B. Gan, G. Buzsáki, Forty-hertz light stimulation does not entrain native gamma oscillations in Alzheimer's disease model mice. *Nat. Neurosci.* **26**, 570–578 (2023).

82. M. L. Hines, N. T. Carnevale, The NEURON simulation environment, *Neural Comput.* 9, 1179–1209 (1997).

83. Q. Sun, A. Sotayo, A. S. Cazzulino, A. M. Snyder, C. A. Denny, S. A. Siegelbaum, Proximodistal heterogeneity of hippocampal CA3 pyramidal neuron intrinsic properties, connectivity, and reactivation during memory recall. *Neuron* **95**, 656–672.e3 (2017).

84. T. G. Banke, C. J. McBain, GABAergic input onto CA3 hippocampal interneurons remains shunting throughout development. *J. Neurosci.* **26**, 11720–11725 (2006).

85. F. Fukushima, K. Nakao, T. Shinoe, M. Fukaya, S. Muramatsu, K. Sakimura, H. Kataoka, H. Mori, M. Watanabe, T. Manabe, M. Mishina, Ablation of NMDA receptors enhances the excitability of hippocampal CA3 neurons. *PLOS ONE* **4**, e3993 (2009).

86. Z. Kohus, S. Káli, L. Rovira-Esteban, D. Schlingloff, O. Papp, T. F. Freund, N. Hájos, A. I. Gulyás, Properties and dynamics of inhibitory synaptic communication within the CA3 microcircuits of pyramidal cells and interneurons expressing parvalbumin or cholecystokinin. *J. Physiol.* **594**, 3745–3774 (2016).

87. N. Vladimirov, R. D. Traub, Synaptic gating at axonal branches, and sharp-wave ripples with replay: A simulation study. *Eur. J. Neurosci.* **38**, 3435–3447 (2013).

88. V. K. Y. Ng, R. A. Cribbie, Using the gamma generalized linear model for modeling continuous, skewed and heteroscedastic outcomes in psychology. *Curr. Psychol.* **36**, 225–235 (2017).